



Istituto Nazionale  
di Fisica Nucleare

LABORATORI NAZIONALI DI FRASCATI  
SIS-Pubblicazioni

LNF-08/19(Thesis)

July 18, 2008

## MERGING AND SPLITTING OF CLUSTERS IN THE ELECTROMAGNETIC CALORIMETER OF THE KLOE DETECTOR

Jarosław Zdebik

*Nuclear Physics Department, Jagiellonian University, Cracow, Poland*

### Abstract

The work was carried out in the framework of the KLOE collaboration studying the decays of the  $\phi$  meson produced in the DAΦNE accelerator in the collisions of electron and positron.

The main aim of this thesis was investigation of the influence of the merging and splitting of clusters in decays with the high multiplicity of  $\gamma$  quanta, which are at most biased by these effects. For this aim we implemented the full geometry and realistic material composition of the barrel electromagnetic calorimeter in FLUKA package. The prepared Monte Carlo based simulation program permits to achieve a fast generation of the detector response separately for each interested reaction. The program was used to study the reconstruction efficiency with the KLOE clustering algorithm as a function of the photocathode quantum efficiency.

It was also used to investigate merging and splitting probabilities as a function of the quantum efficiency. The conducted studies indicated that the increase of quantum efficiency does not improve significantly the identification of clusters. The influence of these effects was estimated for  $\eta$  meson decays into  $3\pi^0$  and  $K_{short}$  meson into  $2\pi^0$ .



”The next question was - what makes planets go around the sun? At the time of Kepler some people answered this problem by saying that there were angels behind them beating their wings and pushing the planets around an orbit. As you will see, the answer is not very far from the truth. The only difference is that the angels sit in a different direction and their wings push inward.”

Richard Feynman (1918 - 1988),  
*Character of Physical Law*



# Contents

<b>1</b>	<b>Introduction</b>	<b>7</b>
<b>2</b>	<b>KLOE2 at DAΦNE experimental facility</b>	<b>9</b>
2.1	DAΦNE collider . . . . .	9
2.2	KLOE detector . . . . .	11
2.2.1	Drift Chamber . . . . .	11
2.2.2	Electromagnetic Calorimeter . . . . .	12
2.2.3	Upgrade of the KLOE detector . . . . .	13
<b>3</b>	<b>Simulation tools</b>	<b>16</b>
3.1	Vertex generator . . . . .	16
3.2	FLUKA - a multi-particle Monte Carlo transport code . . . . .	17
3.3	Implementation of the calorimeter material composition in FLUKA . . . . .	18
3.4	Implementation of the whole geometry of the barrel calorimeter in FLUKA . . . . .	20
3.5	Simulations of the photomultipliers response . . . . .	23
3.6	Description of the KLOE clustering algorithm . . . . .	25
<b>4</b>	<b>Adjustment of the detector properties in simulations</b>	<b>26</b>
4.1	Preparation of the data sample ( $e^+e^- \rightarrow \phi \rightarrow \eta\gamma \rightarrow 3\gamma$ ) . . . . .	26
4.2	Determination of the simulation parameters . . . . .	27
4.2.1	Estimation of the attenuation length of the scintillating fibers . . . . .	27
4.2.2	Parametrization of the energy threshold function . . . . .	32
4.2.3	Calibration of the ionization deposits . . . . .	33
<b>5</b>	<b>Estimations of background due to the merging and splitting of photon clusters</b>	<b>36</b>
5.1	Merging of clusters from $\eta \rightarrow 3\pi^0$ as a background for the $\eta \rightarrow \pi^0\gamma\gamma$ channel . . . . .	36
5.2	Splitting of clusters for $K_S \rightarrow 2\pi^0$ as a background for $K_S \rightarrow 3\pi^0$ . . . . .	39
5.3	Reconstruction efficiency with the KLOE clustering algorithm . . . . .	42
5.4	Reconstruction efficiency as a function of the photocathode quantum efficiency . . . . .	43
5.5	Merging and splitting probabilities as a function of the quantum efficiency . . . . .	44
<b>6</b>	<b>Conclusions</b>	<b>46</b>
<b>A</b>	<b>Kinematic fit procedure</b>	<b>47</b>
<b>B</b>	<b>Monte Carlo Methods</b>	<b>47</b>
<b>C</b>	<b>Energy distributions for <math>\gamma</math> quanta</b>	<b>48</b>
<b>D</b>	<b>Time distribution for single and multi-gamma hits</b>	<b>50</b>
<b>E</b>	<b>Estimation of probability for multi-gamma hits at a single calorimeter module</b>	<b>53</b>

<b>F</b>	<b>Example of the event reconstruction for <math>e^+e^- \rightarrow \phi \rightarrow \eta\gamma \rightarrow 3\pi^0\gamma \rightarrow 7\gamma</math> reaction</b>	<b>56</b>
<b>G</b>	<b>Energy deposition as a function of azimuthal angle</b>	<b>57</b>
<b>H</b>	<b>Definition of the coordinate system</b>	<b>59</b>
	<b>Acknowledgment</b>	<b>63</b>
	<b>References</b>	<b>65</b>

## 1 Introduction

Nowadays, elementary particles and interactions among them are described in the framework of the Quantum Mechanics and Standard Model. Tests of these theories and of fundamental symmetries like C, P, T and their combinations are therefore crucially important for understanding the phenomena in the world of particles [1]. Experiments aiming at the determination of the particle properties and search for processes beyond the applicability of the domain of the Standard Model are conducted in many particle physics laboratories.

Such studies are carried out also in the Laboratori Nazionali Di Frascati (LNF) by means of the electron-positron collider DAΦNE and the KLOE detector setup. The KLOE group has taken data at the colliding electron-positron center-of-mass energy corresponding to the  $\phi$  meson mass. The main objectives of the KLOE experimental program are: investigations of the decays of kaons produced in pairs from the decays of the  $\phi$  meson, the radiative decays of the  $\phi$  meson, the rare branching ratios of the  $\eta$  meson and the light mesons particle properties. One of the interesting example for the pseudoscalar mesons decay is the G-symmetry violating  $\eta \rightarrow \pi^0\gamma\gamma$  process whose branching ratio cannot be described neither in the framework of the Chiral Perturbation Theory nor by the Vector Meson Dominance Model.

At present KLOE detector is being upgraded in order to improve the possibility of the reconstruction of the decays of the  $K_S$  mesons. In particular in order to investigate a CP-violating  $K_S \rightarrow 3\pi^0$  decay [2].

The  $\eta \rightarrow \pi^0\gamma\gamma$  and  $K_S \rightarrow 3\pi^0$  are examples of highly interested channels which are however very challenging to study experimentally due to the large number of the  $\gamma$  quanta in the final state. This fact is caused by difficulties of the rejection of background channels due to merging and splitting of clusters [3]. For example, for the first mentioned reaction a background channel is  $\eta \rightarrow 3\pi^0$  with two merged clusters leading to the same topology as in the case of the  $\eta \rightarrow \pi^0\gamma\gamma \rightarrow 4\gamma$ . And in the case of the  $K_S \rightarrow 3\pi^0$  the background constitutes a  $K_S \rightarrow 2\pi^0$  reaction with two splitted clusters.

In this diploma thesis we investigate the influence of the merging and splitting of clusters on decays with the high multiplicity of  $\gamma$  quanta, which are at most biased by these effects. For this aim we implemented the full geometry and realistic material composition of the barrel electromagnetic calorimeter into FLUKA package. The prepared Monte Carlo based simulation program permits to achieve a fast generation of the detector response separately for each interested reaction.

In chapter 2 we will describe the DAΦNE collider and the KLOE detector.

Chapter 3 comprises description of the vertex generator, used to simulate the kine-

matics of physical decays, and the description of the physics models used by the FLUKA Monte-Carlo program for the generation of nuclear, hadronic and electromagnetic reactions. This chapter includes also description of implementation of materials composition and geometry of the barrel calorimeter in the FLUKA Monte Carlo.

Chapter 4 presents a calibration of the DIGICLU program used for the reconstruction of the photomultiplier response and for the cluster recognition. This chapter includes: i) preparation of the data sample for  $e^+e^- \rightarrow \phi \rightarrow \eta\gamma \rightarrow 3\gamma$  reaction, ii) estimation of the attenuation length for scintillating fibers, iii) calibration of ionization deposits and implementation of the threshold formula to the source code.

In chapter 5 we describe effects of merging of clusters for  $\eta \rightarrow 3\pi^0$  as a background for the  $\eta \rightarrow \pi^0\gamma\gamma$  channel and splitting of clusters for  $K_S \rightarrow 2\pi^0$  as a background for  $K_S \rightarrow 3\pi^0$  reaction. Further on reconstruction efficiency with the KLOE clustering algorithm as a function of the photocathode quantum efficiency is presented. Finally, merging and splitting probabilities as a function of the quantum efficiency are studied.

Chapter 6 summarises the whole thesis and brings the conclusions and remarks.

This thesis is supplemented with appendics where section A presents a kinematic fit procedure and section B generally describes Monte Carlo Methods. In appendix C energy distribution for  $\gamma$  is presented. Section D presents a time distribution for single and multi-gamma hits. The sections E and F contain an estimation of probability for multi-gamma hits at a single calorimeter module and example of the event reconstruction for the process  $e^+e^- \rightarrow \phi \rightarrow \eta\gamma \rightarrow 3\pi^0\gamma \rightarrow 7\gamma$ , respectively. The G section comprises a description of the energy deposition in the barrel calorimeter as a function of azimuthal angle and the last section presents definition of the used coordinate system.

## 2 KLOE2 at DAΦNE experimental facility

The KLOE (**K**long **E**xperiment) detector is installed at the interaction point of the electron and positron beams of the DAΦNE (**D**ouble **A**nnular  $\phi$ -factory for **N**ice **E**xperiments) collider operating in the Laboratori Nazionali di Frascati (LNF).

It has been designed with the primary goal to measure the CP violation parameter  $R(\frac{\epsilon'}{\epsilon})$  [4] with a sensitivity of one part in ten thousand by using the double ratio method [5].

This detector was fully constructed by the end of the year 1998 [1], and since then it was taking data for seven years. The experimental program was completed with integrated luminosity of  $2.5 \text{ fb}^{-1}$  obtained predominantly with the center-of-mass energy equal to the mass of the  $\phi$  meson ( $\sqrt{s} \sim M_\phi = 1019.456 \pm 0.020 \text{ MeV}$  [6]).

Table 1: Main decays of the  $\phi$  meson [59].

Decay	BR(%)
$\phi \rightarrow K^+ K^-$	49.1
$\phi \rightarrow K_S K_L$	33.8
$\phi \rightarrow \rho\pi / \pi^+ \pi^0 \pi^-$	15.6
$\phi \rightarrow \eta\gamma$	1.26

The cross section for the production of the  $\phi$  vector meson is large and amounts to  $\sigma(e^+e^- \rightarrow \phi) = 3.1 \text{ } \mu\text{b}$ .

The  $\phi$  meson decays predominantly into pairs of neutral or charged kaons (see Table 1).

### 2.1 DAΦNE collider

DAΦNE at Frascati consists of two intersecting crossing accelerator rings, one for positrons and one for electrons. The main DAΦNE parameters are presented in Table 2, and scheme of the facility is shown in Fig. 1.

Table 2: The main characteristics of the DAΦNE collider [7].

Parameter	Value
Energy [GeV]	0.51
Trajectory length [m]	97.69
RF frequency [MHz]	368.26
Bunch length [cm]	1-3
Number of colliding bunches	111
Emittance, $\epsilon_x$ [mm·mrad]	0.34

Positrons and electrons are accelerated in the LINAC (**L**inear **A**ccelerator) which delivers electron or positron beams in the energy range from 25 to 725 MeV with intensities varying from  $10^{10}$  particle per pulse down to a single-electron [7]. This 60 meters long accelerator is the heart of the DAΦNE injection system. It is an S-band machine (2.865 GHz) which delivers 10 ns pulses at a repetition rate of 50 Hz. Electrons, after acceleration to final energy in the LINAC, are accumulated and cooled in the accumulator and transferred to a single bunch into ring. Positrons require first accelerating of electrons to about 250 MeV to target in the LINAC, where positrons are created. Afterwards the positrons follow the same accelerator elements as electrons [1]. Positrons and electrons after acceleration and accumulation process run around in two storage rings and hit in the collision points. This facility is called a Frascati Φ-Factory complex because it was able to produce about 3.3 billions of  $\phi$  mesons during the years from 2000 to 2005. The KLOE experiment was located in one of the two collision points at DAΦNE collider, whereas the second collision point was alternatively occupied by two other experiments: DEAR [8] and FINUDA [9].

At present a new  $e^+e^-$  interaction region is being constructed [10] in order to increase the collider luminosity up to an order of magnitude, from  $10^{32}\text{cm}^{-1}\text{s}^{-2}$  to  $\approx 10^{33}\text{cm}^{-1}\text{s}^{-2}$  [3].

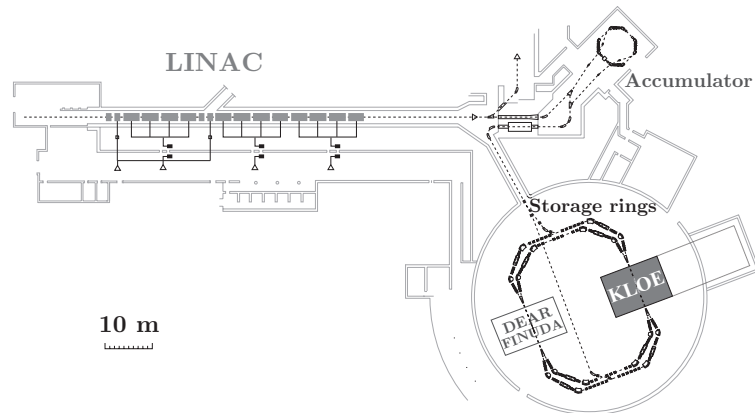


Figure 1: Scheme of the DAΦNE collider. The figure is adapted from [1].

At the interaction point (IP) the beam pipe has the shape of a sphere which is made of a beryllium-aluminium alloy with 10 cm diameter and  $50\ \mu\text{m}$  thickness. The beryllium, having a low atomic number, has been used to minimize the interaction of particles produced at the interaction point with the beam pipe material [6].

## 2.2 KLOE detector

The KLOE detector, which is shown schematically in Fig. 2, was designed for the study of CP violation in the neutral-kaon system. It consists of two main elements: i) an electromagnetic calorimeter (EmC) [11] for the detection of  $\gamma$  quanta, charged pions and  $K_L$  mesons and ii) a large drift chamber (DC) [12] for the measurement of charged particles trajectories [13]. The drift chamber and the calorimeter are inserted in the field of the superconducting coil which produces a magnetic field parallel to the beam axis [11]. The field intensity is equal to 0.52 T [6].

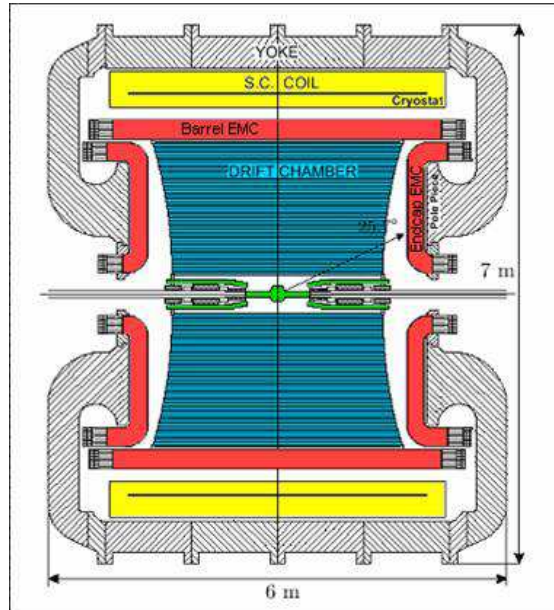


Figure 2: The KLOE detector. For the description see text. The figure is adapted from [3].

The radius of the active part of the KLOE detector is two meters. This size enables to register about 40% decays of neutral long-lived kaons [1]. In the near future KLOE will be upgraded by inner tracker and  $\gamma\gamma$  tagger in order to improve its tracking capabilities [3].

### 2.2.1 Drift Chamber

The KLOE Drift Chamber (DC) [12] consists of 12582 drift cells ( $2 \times 2$ ,  $3 \times 3$   $cm^2$ ) arranged in 58 cylindrical layers surrounding the beam pipe. The diameter and length of the DC is equal to 4 m and 3.3 m, respectively [14]. It is filled with 90% helium and 10% isobutane gas mixture, giving a radiation length (gas + wires) equal to 900 m. Charged particles traveling through the drift chamber are ionizing gas medium and then electrons

created along the particle trajectory drift to the wires with positive voltage. A multiplication mechanism causes detectable signal at the wire's end [1]. The DC measures the  $K_{L,S}$  charged vertex with  $\sim 1$  mm accuracy. It provides fractional momentum resolution of  $\frac{\sigma_p}{p} \sim 0.5\%$  for low momentum tracks. It is transparent to  $\gamma$  down to 20 MeV and limits to acceptable levels the  $K^0$  regeneration and  $K^\pm$  multiple scattering.



Figure 3: Photo of the KLOE drift chamber. The figure is adapted from [15].

The hit position resolution is  $150 \mu\text{m}$  in the central part of the cell, increasing close to the wire and towards the cell boundary. The spatial resolution in the " $\phi$  coordinate" (azimuthal angle) is well below  $200 \mu\text{m}$ . The hit identification efficiency is larger than 99%, whereas the efficiency for associating an existing hit to track amounts to about 97% [14].

### 2.2.2 Electromagnetic Calorimeter

The KLOE calorimeter is made of the lead layers with about 1,2 mm thickness (200 layers per 1 module) which are filled with scintillating fibers of 1 mm diameter. The whole electromagnetic calorimeter (EmC) consists of three main parts: barrel and two endcaps. Barrel (Fig. 4) is composed of 24 modules with trapezoid shape of 23 cm thickness aligned with the beams and surrounding the drift chamber detector. Endcaps are situated over the magnet pole pieces (see Fig. 2) and hermetically close the calorimeter with 98% of  $4\pi$  [1]. Each of the two endcaps calorimeters consists of 32 vertical modules with length ranging from 0.7 to 3.9 meters. The endcap modules are bent and their cross-section with plane parallel to the beam axis is rectangular with thickness of 23 cm [16].

The volume of the calorimeter consists of 50% fiber, 40% lead and 10% of glue. The measured performances for this detector are: full efficiency for  $\gamma$  quanta from 20 to 500 MeV [14],  $\sigma(x) \sim 1$  cm,  $\sigma(E) \sim \frac{5.7\%}{\sqrt{E(\text{GeV})}}$ ,  $\sigma(t) \sim \frac{54 \text{ ps}}{\sqrt{E(\text{GeV})}}$ .

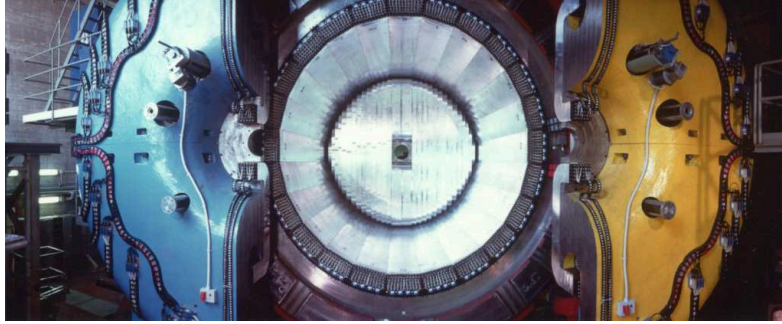


Figure 4: Photo of the KLOE calorimeter. One sees 24 modules of the barrel and the inner plane of the endcap. The figure is adapted from [15].

### 2.2.3 Upgrade of the KLOE detector

At present the KLOE detector is being upgraded in view of the new experimental program which will extend the studies to the more precise measurement of the  $K_S$  mesons and the production of meson in the  $\gamma\gamma$  fusion [3]. For this aim a vertex detector and the  $\gamma\gamma$ -tagger [17] are being built [26].

#### Vertex Detector

In the KLOE detector the first hit was measured by drift chamber at a radius of 28 cm from the interaction point (IP) [3]. Therefore in order to improve the resolution of the determination of the  $K_S$  and  $K_L$  decay near the interaction point a new vertex detector is constructed [17]. This detector consists of five concentric layers of cylindrical triple-GEM (C-GEM), completely realized with very thin polyimide foils [20–22,18,19]. The scheme of the vertex detector is presented in Fig. 5.

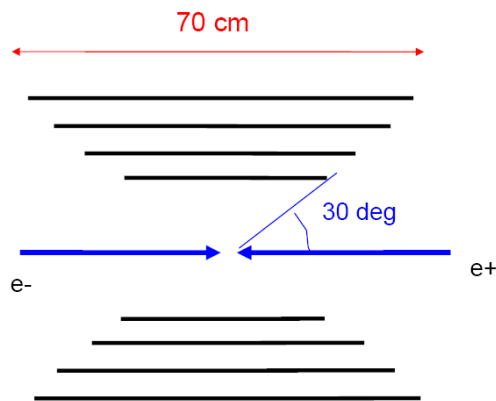


Figure 5: Schematic view of the vertex detector. The figure is adapted from [3].

It will be made of light materials in order to minimize  $\gamma$  absorption. The resolution on  $r$ - $\phi$  surface is expected to be around  $200 \mu\text{m}$  and on  $z$  coordinate about  $500 \mu\text{m}$  [23].

### $\gamma\gamma$ tagger

The main task of this detector is the detection of  $e^+$  and  $e^-$  from  $\gamma\gamma$  reactions emitted at small angle [23,43] with the widest possible energy ranges.  $\gamma\gamma$  tagger will provide information on the angle and the energy of the scattered electrons and positrons [24] and hence it will permit to study the production of mesons in  $\gamma\gamma$  fusion via the reaction:

$$e^+e^- \rightarrow e^+e^-\gamma^*\gamma^* \rightarrow e^+e^- + X, \quad (1)$$

where  $X$  is some arbitrary final state allowed by conservation laws. The tagger consists of microstrip silicon detector and plastic scintillator hodoscope.

### New QCAL

The upgrade of QCAL detector (Fig. 6) [25] was needed, because the interaction region was modified and in the present scheme the angle between colliding beams has been increased from 8 to 18 degrees, which practically excludes the possibility to use the existing QCAL calorimeter [26]. The schematic view of upper part of the previous QCAL detector is presented in Fig. 6.

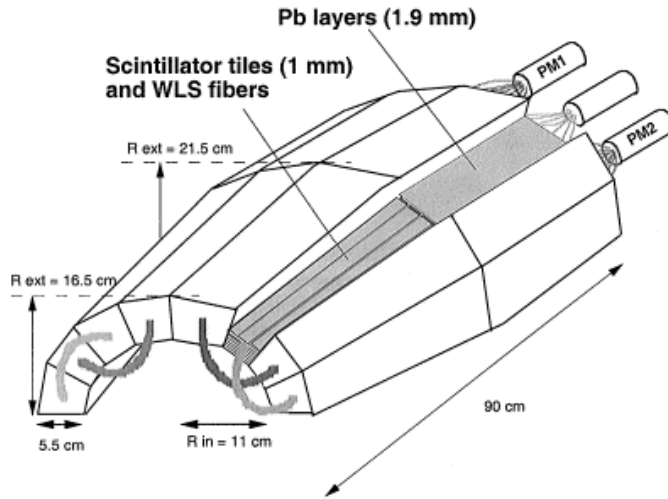


Figure 6: Schematic view of the QCAL detector. The figure is adapted from [25].

The upgraded detector, with improved position resolution, will allow to extend the search for  $K_L \rightarrow 2\pi^0$  events also in case when three photons are reconstructed in the EmC

and one photon in QCALT, thus strongly reducing the correction for acceptance [26] and the contamination from  $K_L \rightarrow 3\pi^0$  when some photons hit the detector.

### 3 Simulation tools

In this chapter we will describe tools used for simulations of signals in the EmC. To compute the physical response of the barrel calorimeter we applied the following programs: i) VERTEX GENERATOR which simulates kinematics of the physical reactions ii) FLUKA package which reproduces particle interaction, propagation and a realistic light output in the scintillating fibers, and iii) DIGICLU reconstruction program which simulates the response of photomultipliers and reconstructs energy and time for particles hitting the calorimeter. FLUKA package is mostly used for low energy physic, like: hadronic interactions, medical science, neutrino beam simulation or in dosimetry science. Using FLUKA we can achieve accurate description of the physics processes in the KLOE detector.

#### 3.1 Vertex generator

In order to enable a fast simulations of the meson decays in the KLOE detector we have prepared a "vertex generator" for simulations of the final state momenta of the decay products<sup>1</sup>. This program is compatible with FLUKA Monte Carlo and simulates decays of  $\phi$  meson to channels with  $\eta$ ,  $\eta'$  and kaons. It is based on the CERN library procedure GENBOD which generates four-momentum vectors of particles in the final state which are homogenously distributed in the phase space [27]. This tool permits to calculate four-momenta of final state particles in the rest frame of the decaying object. Additionally we implemented an angular distribution ( $\frac{1+\cos^2\theta}{2}$ ) for  $\gamma$  quanta from the radiative  $\phi$  meson decay ( $\phi$  is a vector meson with spin = 1). At present, for the purpose of this work the generator can simulate six below listed reactions:

1.  $e^+e^- \rightarrow \phi \rightarrow \eta\gamma \rightarrow 3\gamma$ ,
2.  $e^+e^- \rightarrow \phi \rightarrow \eta\gamma \rightarrow 3\pi^0\gamma \rightarrow 7\gamma$ ,
3.  $e^+e^- \rightarrow \phi \rightarrow \eta'\gamma \rightarrow 3\gamma$ ,
4.  $e^+e^- \rightarrow \phi \rightarrow \eta'\gamma \rightarrow 3\pi^0\gamma \rightarrow 7\gamma$ ,
5.  $e^+e^- \rightarrow \phi \rightarrow K_S K_L$ ,
6.  $e^+e^- \rightarrow \phi \rightarrow \pi^0\gamma \rightarrow 3\gamma$ .

It is however constructed in a way which enables an easy implementation of any further process.

---

<sup>1</sup>In our group this generator is called jjpluto.

### 3.2 FLUKA - a multi-particle Monte Carlo transport code

This section is based on the informations given in references [29,32]. FLUKA is a multipurpose transport Monte Carlo code, able to treat hadron-hadron, hadron-nucleus, neutrino, electromagnetic, and  $\mu$  interactions up to 10000 TeV [28]. Also the transport of the charged particles is well recreated (handled in magnetic field too). This Monte Carlo is based, as far as possible, on original and well tested microscopic models. Due to this "microscopic" approach to hadronic interaction modelling, each step is self-consistent and has well confirmed physical bases [28]. FLUKA can be used in realistic simulations involving following physical effects:

**Hadron inelastic nuclear interactions** - are based on resonance production and decay below a few GeV, and above on the Dual Parton model. FLUKA can also simulate photo-nuclear interactions (described by Vector Meson Dominance, Delta Resonance, Quasi-Deuteron and Giant Dipole Resonance models) [29].

**Elastic Scattering** - this process is accomplished with tabulated nucleon-nucleus cross sections. Tabulated are also phase shift data for pion-proton and for kaon-proton scattering [29]. To this Monte Carlo also parametrised nucleon-nucleon cross-sections were implemented.

**Nucleus-Nucleus interactions** - are treated through interfaces to external event generators. From 0.1 to 5 GeV per nucleon a modified RQMD is used, whereas for higher energies DPMJET generator is applied [30].

**Transport of charged hadrons and muons** - a code can handle electron backscattering and energy deposition in thin layers even in the few keV energy range. The energy loss is simulated with Bethe-Bloch theory with account for spin effects and ionisation fluctuations [29].

**Low-energy neutrons** - for neutrons with energy lower than 20 MeV, FLUKA uses neutron cross-section library, containing more than 140 different materials. The transport of these particles is realised by simulation of the standard multigroup transport with photon and fission neutron generation [29]. Detailed kinematics of elastic scattering on hydrogen nuclei is implemented too.

**Electrons** - FLUKA uses an original transport algorithm for charged particles, including a complete multiple Coulomb scattering treatment giving the correct lateral displacement even near boundary. The Landau-Pomeranchuk-Migdal suppression effect and the Ter-Mikaelyan polarisation effect in the soft part of the bremsstrahlung spectrum are also implemented. Electrons are propagated taking into account a positron annihilation in flight and Möller scattering effects.

**Photons** - to reproduce photons physics the following effects were implemented

to this Monte Carlo: pair production with actual angular distribution of electrons and positrons, Rayleigh scattering, photon polarisation effect, photo-hadron production, Compton effect with account for atomic bonds through use of inelastic Hartree-Fock form factors.

**Optical photons** - generation and transport is based on Cherenkov, Scintillation and Transition Radiation.

**Neutrinos and muons** - FLUKA package includes also cosmic ray physics [31] and can simulate muons and neutrinos interactions. This tool is used for basic research and applied studies in space and atmospheric flight dosimetry and radiation damage [31]. Interactions are implemented independly of tracking procedures [29]. By default they are tracked without interactions [29].

### 3.3 Implementation of the calorimeter material composition in FLUKA

The Monte Carlo code FLUKA is used to determine the position, time and energy of the ionization deposits in the fibers caused by particles hitting the calorimeter. We used the FLUKA "lattice" tool to design the fiber structure of the calorimeter module [32]. In the base module the calorimeter is simulated in detail (see Fig. 7), both under the geometrical point of view and with respect to the used materials.

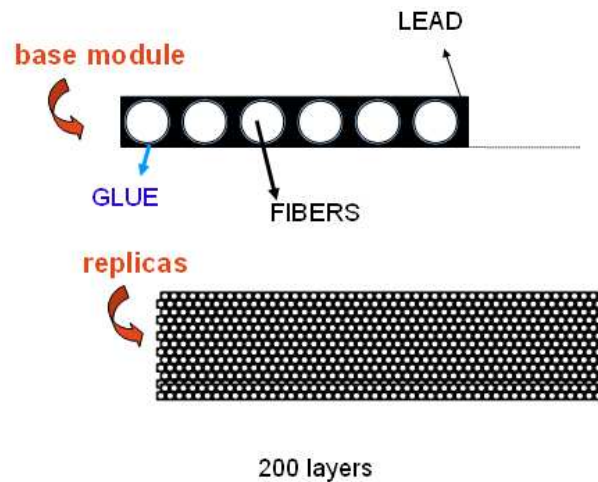


Figure 7: Details of the implementation of the calorimeter layers [33].

The calorimeter is built out of lead, plexi and glue [34] which are composed as follows:

- lead compound is made of Pb (95%) and Bi (5%),
- the scintillating fibers are made of Polystyrene ( $C_2H_3$ ),

- the glue is a mixture of the epoxy resin ( $C_4H_4O$ ,  $\rho = 1.14 \text{ g/cm}^3$ ) and hardener ( $\rho = 0.95 \text{ g/cm}^3$ ) constituting 72% and 28% of the mixture, respectively.

The hardener has been simulated as a mixture of several materials which composition is given in Table 3.

Table 3: Composition of the hardener mixture [34].

Compound	formula	fraction
Polyoxypropyldiamine	$C_7H_{20}O_3$	90%
Triethanolamine	$C_6H_{15}O_3$	7%
Aminoethylpiperazine	$C_6H_{15}N_3$	1.5%
Diethylenediamine	$C_4H_{10}N_2$	1.5%

The module consists of two types of scintillating fibers: "Kuraray" and "Pol.hi.tech". The first are implemented until a depth of 12 cm and the remaining part of the module is built with "Pol.hi.tech" fibers [34]. A proper attenuation length parameter for fibers material in order to calculate a light intensity at each side of the module was taken into account. The attenuation function of fibers was described with the following formula [34]:

$$B = A \cdot e^{-\frac{y}{\lambda_1}} + (1 - A) \cdot e^{-\frac{y}{\lambda_2}}, \quad (2)$$

where  $y$  is distance between the place of deposited energy and the photocathode. The attenuation factor  $B$  is the ratio between detected and generated light signal which changes as a function of the distance (on  $y$  axis) from the generation point to the photocathode. The value of the parameters for "Kuraray" and "Pol.hi.tech" are shown in Table 4.

However, it is worth mentioning that, as we will show in the next chapters the data can be also well described using this formula but with only one exponential function.

Table 4: Fibers parameters.

	A	$\lambda_1$ cm	$\lambda_2$ cm
Kuraray	0.35	50	430
Pol.hi.tech	0.35	50	330

The energy deposits are computed by FLUKA [35] taking into account the Birks effect [36] (see equation 3), that is the saturation of the light output ( $L$ ) of a scintillating material when the energy release is high [35]. For high densities of energy deposition, due to the quenching interactions between the excited molecules along the path of incident particles, the light output is not changing linearly with the energy deposition but instead it can be described as [37–40]:

$$\frac{dL}{dx} = \frac{k \cdot \frac{dE}{dx}}{\left[1 + c_1 \cdot \frac{dE}{dx} + c_2 \cdot \left(\frac{dE}{dx}\right)^2\right]}, \quad (3)$$

This law describes the light output of (organic) scintillators [40,39]. The "k" constant depends on the particle type, and is in the order of  $0.01 \text{ g cm}^2 \text{ MeV}^{-1}$ , and the parameters  $c_1$  and  $c_2$  are equal to [33,41,42]:

$$\begin{aligned} c_1 &= 0.013 \text{ cm}^2 \text{ MeV}^{-1}, \\ c_2 &= 9.6 \times 10^{-6} \text{ cm}^3 \text{ MeV}^{-2}. \end{aligned}$$

### 3.4 Implementation of the whole geometry of the barrel calorimeter in FLUKA

FLUKA simulation package is mostly used in low energy physics, for example in: medical science, dose evaluation, neutron beam simulation and for simulations of the low energy hadronic interactions. Therefore, the program is especially suited for simulations of the response of the KLOE electromagnetic calorimeter, because at KLOE experiment we deal with particles in the rather low energy range up to 1 GeV.

The main idea for implementation of the geometry of the KLOE detector with FLUKA was proposed by Giuseppe Battistoni [44]. It was first realized for one calorimeter module with rectangular shape<sup>2</sup>, with accurate description of materials. The base cell with dimensions of  $52 \text{ cm} \times 1.2 \text{ mm} \times 430 \text{ cm}$  consists of the lead block filled with 385 scintillating fibers and glue cylinders. This cell was replicated 199 times (using FLUKA lattice tool) to build 200 layers forming the calorimeter module (see left panel in Fig. 8).

Our first step in the way to implement the whole barrel of electromagnetic calorimeter into FLUKA was the extension of the rectangular module to the realistic trapezoid shape. This was achieved by declaration of a new base cell consisting of a scintillating fiber and glue cylinder both inserted into a small block of lead. The length of the cell is equal to the length of the module (4.3 m) and its cross section corresponds to the square of 1.2 mm, where the fiber diameter is equal to 1 mm and width of the glue cylinder equals to 0.1 mm. Then this new base cell was replicated about 4000 times to build two triangular sections on the left and right side of the module. A complete visualisation of the new trapezoid geometry<sup>3</sup> is shown in Fig. 8. In order to raise our confidence to the functioning of the programs we have simulated energy deposits in a single calorimeter module for the reaction:  $e^+e^- \rightarrow \phi \rightarrow \eta\gamma \rightarrow 3\pi^0\gamma \rightarrow 7\gamma$ .

<sup>2</sup>Implementation to FLUKA package was done by: G. Battistoni, B. Di Micco, A. Ferrari, A. Passeri and V. Patera.

<sup>3</sup>Visualization is based on the FLUKA sources and prepared using a FLAIR (FLUKA advanced visualization geometry tool) [45].

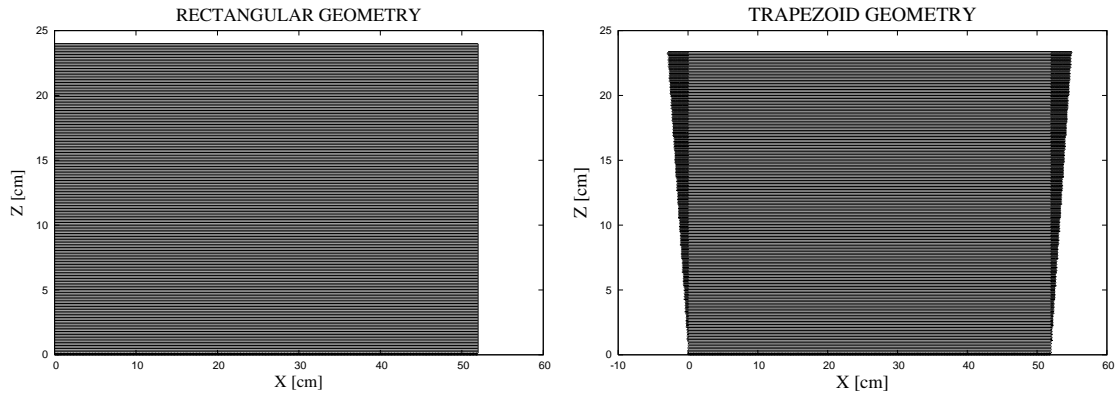


Figure 8: Cross section of the EmC module with rectangular and trapezoid geometry. Visualization by the FLAIR program [45] using as an input a geometry setup files of FLUKA.

The results of these simulations for 20000 events are shown in Fig. 9.

A trapezoid structure which was built with a realistic light output from the scintillating fibers can be easily recognized. One can also see that as expected the most energy deposits are observed in the bottom part of the module.

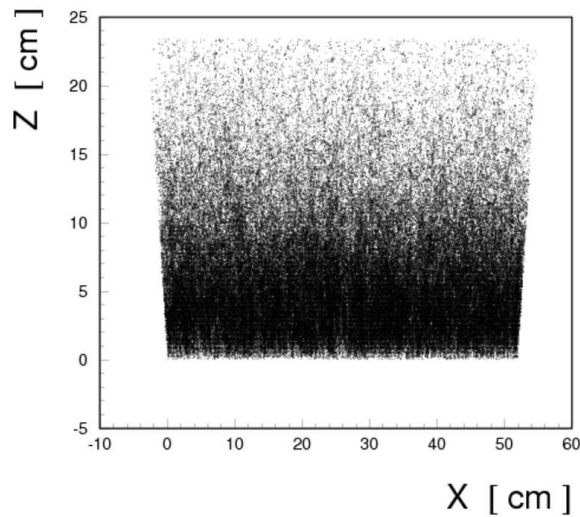


Figure 9: Distribution of energy deposits in scintillating fibers of a single unit of the electromagnetic calorimeter.

As a next step, it would be natural to replicate 23 times the defined geometry for one module and to build a full barrel of the electromagnetic calorimeter. This task was unfor-

Unfortunately impossible to realize with present version of FLUKA<sup>4</sup> [32] because this version doesn't permit to replicate the region which had been replicated before. It is due to the fact that the lattice replication on the second and higher levels is not implemented yet. This is the reason why geometry was built in another, unfortunately much more complicated way.

The barrel was first defined as 24 empty volumes (containers). In one of these volumes we implemented the base cell which described one layer of lead, fibers and glue. This cell was replicated 199 times in this volume, to build a rectangular section part of the main trapezoid module (on the top in Fig. 10)<sup>5</sup>, and these base cell was replicated 200 times in each of the remaining 23 modules. Next in the first module we filled the full structure of lead, fibers and glue cylinder in the two triangle areas. These two regions were then replicated at the corresponding positions in the remaining modules [46].

Fig. 10 shows a visualisation of the whole barrel calorimeter geometry made with FLAIR [45]. The left panel of the next figure presents details of the edge area, between base module on the top and the first replicated area on the right side of it.

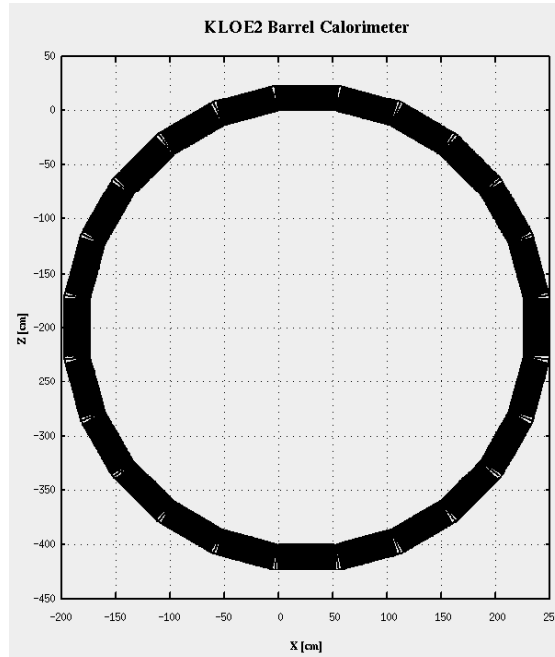


Figure 10: Visualization of the 24 trapezoid modules of the barrel calorimeter with FLAIR.

In the right panel of Fig. 11 the energy deposits in scintillating fibers for this area are presented for  $e^+e^- \rightarrow \phi \rightarrow \eta\gamma \rightarrow 3\pi^0\gamma \rightarrow 7\gamma$  reaction with statistics of 1000 events.

<sup>4</sup>FLUKA 2006 for GNU linux operating system.

<sup>5</sup>The same idea was used to build a single module with rectangular shape.

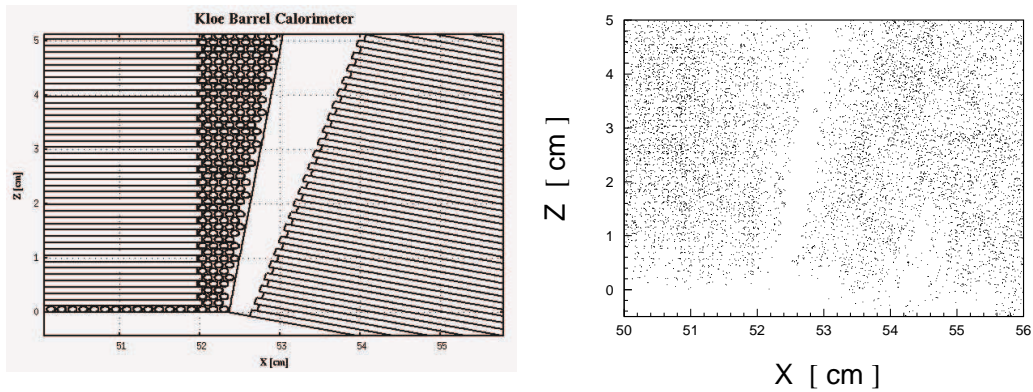


Figure 11: Details of the implementation on the edge of two modules.

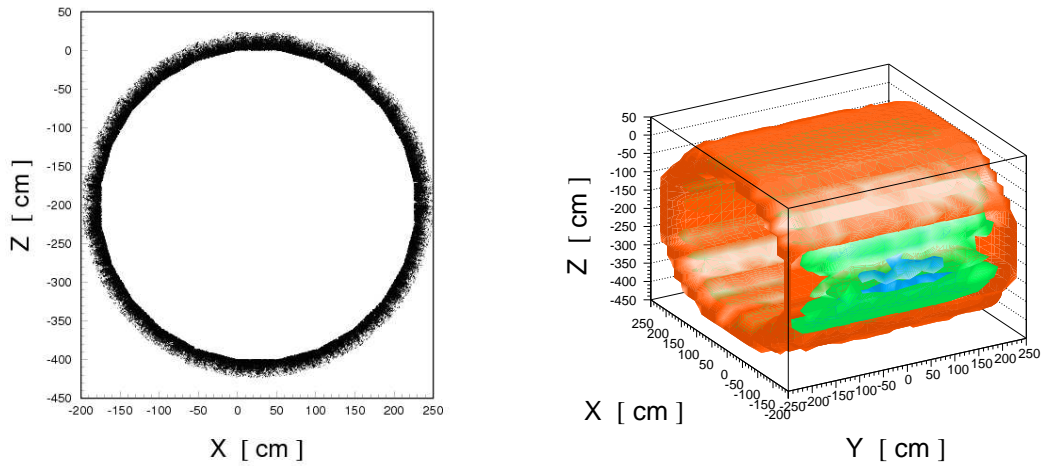


Figure 12: Energy depositions in fibers in the KLOE barrel calorimeter.

Using this geometry we are able to study in details energy deposits also at the edges of the modules of the calorimeter, where there are small areas without fibers [47,48].

Finally in Fig. 12, as an example of the proper implementation of the geometry we show energy deposits in scintillating fibers in the whole barrel calorimeter.

### 3.5 Simulations of the photomultipliers response

After simulation of energy deposits in scintillating fibers with FLUKA program we calculated amplitude of signals in photomultipliers using DIGICLU program. This program also enables to reconstruct the time, position and energy for all readout segments

(cells) of each calorimeter module [11]. Each module is divided into 60 cells which are situated in 5 layers and 12 columns (see Fig. 13). Each cell is read out on both sides by photomultipliers. This segmentation provides the determination of the position of energy deposits in the calorimeter. Altogether, the barrel calorimeter consists of 1440 cells, which are read out by photomultipliers on two sides (referred to as side A and side B in the following).

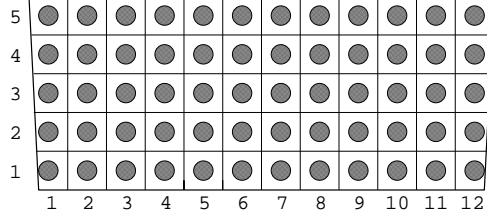


Figure 13: Schematic view of the readout cells structure on the one side of the barrel module. Filled circles represent photomultipliers.

For each cell two time signals  $T^A, T^B$  (digitized by the Time to Digital Converter (TDC)) and two amplitude signals  $S^A, S^B$  (measured by Analog to Digital Converter (ADC)) are recorded. The arrival time  $t$  and position  $s$  of the impact point along the fiber direction (the zero being taken at the fiber center) is calculated with the aid of times measured at two ends as:

$$t(ns) = \frac{1}{2}(t^A + t^B - t_0^A - t_0^B) - \frac{L}{2v}, \quad (4)$$

$$s(cm) = \frac{v}{2}(t^A - t^B - t_0^A + t_0^B), \quad (5)$$

with  $t^{A,B} = c^{a,b} \cdot T^{A,B}$ , where  $c^{A,B}$  are the TDC calibration constants,  $t_0^{A,B}$  denotes overall time offsets,  $L$  stands for length of the cell (cm) and  $v$  is the light velocity in fibers (cm/ns). The energy signal is calculated according to the formula:

$$E_i^{A,B}(MeV) = \frac{S_i^{A,B} - S_{0,i}^{A,B}}{S_{M,i}} \cdot K, \quad (6)$$

where  $S_{0,i}$  are the zero-offsets of the amplitude scale,  $S_{M,i}$  corresponds to the response for the minimum ionizing particle crossing the calorimeter center and  $K$  factor gives the energy scale in MeV, and it is obtained from signals of particles with known energy.

The total energy deposited in a cell is calculated as the mean of values determined at both ends for each cell [11]. The energy read-out has been simulated by including both the generation of photoelectrons with the Poisson distribution and the threshold on the constant fraction discriminator.

### 3.6 Description of the KLOE clustering algorithm

As we presented in the previous section the DIGICLU program simulates photomultipliers response and reconstructs energy deposit, position and time for particles passing through each cell. These values are used to recognize groups of cells (clusters) belonging to particles entering the calorimeter. For this aim a clustering algorithm is used [11]. Ideally, to each particle it should assign exactly one cluster but in practice it is not always the case. After the recognition of clusters the program reconstructs the spatial coordinates and time of each shower with high accuracy, needed to reconstruct the decay vertex of the  $K_L$  [49]. In particular the algorithm is based on the following steps. First for each cell the position and energy of the shower is reconstructed. Next preclusters are built by connecting the neighboring cells in time and space in order to recreate a full shower [11]. Cells are taken into account in searching of preclusters only if times and energy signals are available on both sides, otherwise these cells in the most cases are added to the already recognized clusters [6]. Subsequently, preclusters are splitted if the spread of the time of the assigned cells is larger than 2.5 ns. On the other hand cells are merged in one cluster if a distance between them and the center of the precluster is less than 20 cm. After this check the groups of cells are defined as clusters which position and time are computed as energy-weighted averages of the contributing cells.

## 4 Adjustment of the detector properties in simulations

In order to simulate a realistic response of photomultipliers we have adjusted parameters used in the programme by comparing the output of simulations to results from the experimental sample of events identified as  $\phi \rightarrow \eta\gamma \rightarrow 3\gamma$  process.

### 4.1 Preparation of the data sample ( $e^+e^- \rightarrow \phi \rightarrow \eta\gamma \rightarrow 3\gamma$ )

At a first stage, an experimental data sample for the  $e^+e^- \rightarrow \phi \rightarrow 3\gamma$  reaction has been extracted [50] applying the kinematic fit procedure to the 3  $\gamma$  events with the following conditions:

$$\begin{aligned} \sum_{i=1}^3 E_{\gamma_i} &= E_{\phi} , \\ \sum_{i=1}^3 p_{\gamma_i} &= p_{\phi} , \\ t_i - \frac{r_i}{c} &= 0 , \end{aligned} \tag{7}$$

where,  $c$  is the light velocity,  $t_i$  denotes the time of each reconstructed cluster and  $r_i$  stands for the distance from the vertex collision point to the cluster centroid position.  $E_{\phi}$  and  $p_{\phi}$  denote the total energy and momentum of the  $\phi$  meson, respectively. The first and second condition results from energy and momentum conservation rules. The third requirement ensures that we take events which originate only from the collision point.

As a next step, the distributions of the square of the invariant mass for pairs of the  $\gamma$  quanta for  $e^+e^- \rightarrow \phi \rightarrow 3\gamma$  process have been constructed. The results are shown in the left panel of Fig. 14. The numbers were assigned to the  $\gamma$  quanta such that they are ordered according to the increasing energy:  $E_1 < E_2 < E_3$ . Thus  $\gamma_3$  is the photon with the highest energy and  $\gamma_1$  with the lowest. The right panel presents results of simulations for the following reactions:

1.  $e^+e^- \rightarrow \phi \rightarrow \eta\gamma \rightarrow 3\gamma$  ,
2.  $e^+e^- \rightarrow \phi \rightarrow \pi^0\gamma \rightarrow 3\gamma$  ,
3.  $e^+e^- \rightarrow \phi \rightarrow 3\gamma$  .

The blue bevel line and the vertical band at the  $\eta$  mass squared denote signals from the first reaction.

The channel where  $\phi$  meson decays to  $\pi^0\gamma$  is described by the red line with value of

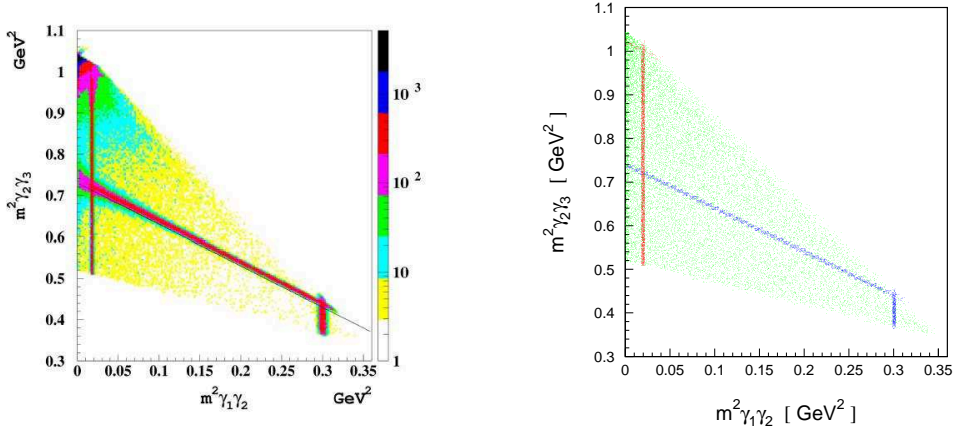


Figure 14: The distribution of the square of the invariant mass for  $\gamma$  pairs from  $e^+e^- \rightarrow \phi \rightarrow 3\gamma$  reaction from the experiment (left panel [50]) and from the simulation (right panel).

$m^2_{\gamma_1\gamma_2}$  equal to 0.018 GeV<sup>2</sup>. And finally the green "triangular" region originates from reactions where  $\phi$  meson decays directly to  $3\gamma$  quanta.

For the further analysis we took all events from the vertical  $\eta$  band which are positioned below the red bevel line (see left panel in Fig. 14) [50].

## 4.2 Determination of the simulation parameters

In this section we describe determination of the attenuation length for the scintillating fibers, determination of the threshold function, and calibration of the ionization deposits in the electromagnetic calorimeter.

### 4.2.1 Estimation of the attenuation length of the scintillating fibers

The first step for estimation of the attenuation length was the selection of events corresponding to the  $\phi \rightarrow \eta\gamma \rightarrow \gamma\gamma\gamma$  reaction and identification of monoenergetic  $\gamma$  from the  $\phi \rightarrow \eta\gamma$  radiative decay. In the next step we simulated the total energy deposited in cells of a given plane as a function of Z coordinate [51].

We used the following selection cuts:

1. Monochromatic photons ( $361 < E_\gamma < 365$  MeV) from  $\phi$  meson decay ,
2.  $|Z_\gamma^{\text{reconstructed}} - Z_\gamma^{\text{generated}}| < 20$  cm .

The first condition guarantees that we take only events with  $\gamma$  quanta from  $\phi$  me-

son decay directly. The second condition guarantees that we take only events where the distance between position where  $\gamma$  quanta hit the module in simulation and reconstructed position of the cluster must be less than 20 cm.

The results for 5 layers are shown in Fig. 15. One can see that distribution of the average energy depositions in cells are not uniform, and therefore for the studies of the attenuation length it is mandatory to divide the experimental data by the Monte Carlo distributions.

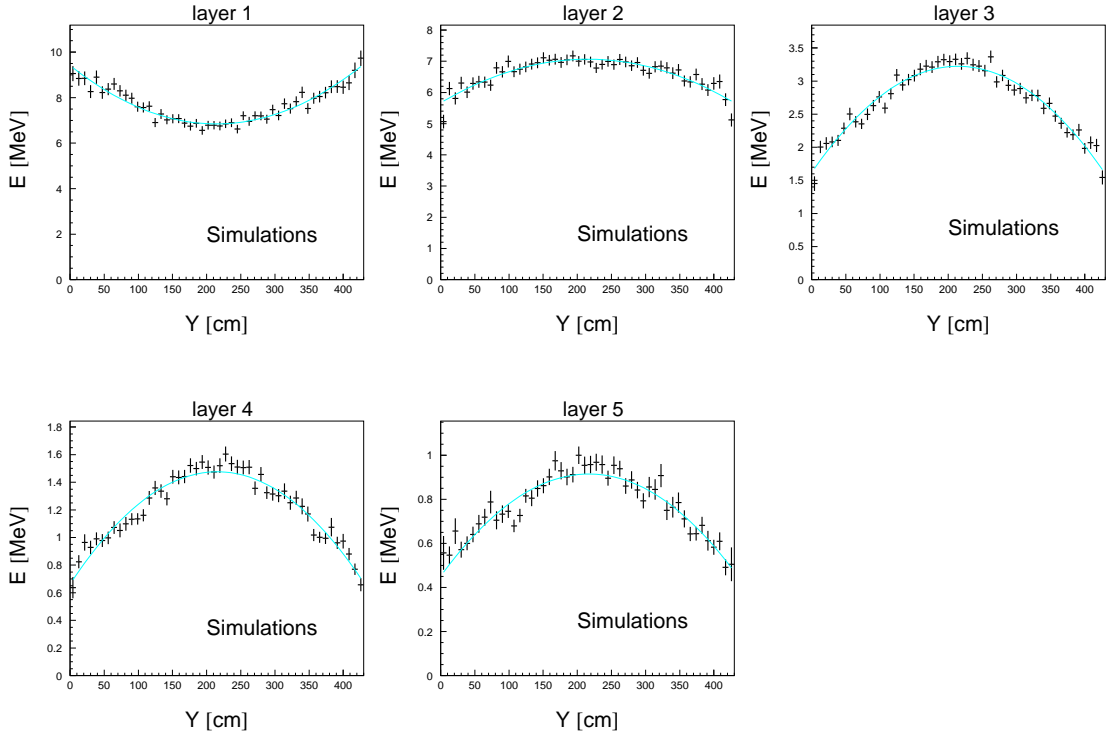


Figure 15: Simulation of the total energy deposits in cells for each of the 5 calorimeter layers for the  $\phi \rightarrow \eta\gamma$  decay. Courtesy of E. Czerwiński and B. Di Micco [54].

In case of the first layer, which is the nearest one with respect to the collision point, the shape of the energy distribution is mostly related (i) with the angular distributions of the  $\gamma$  quanta from the  $\phi \rightarrow \eta\gamma_1 \rightarrow \gamma_1\gamma_2\gamma_3$  decay, (ii) with the changes of the solid angle distribution along the module, and (iii) with the change of the input angle into calorimeter surface. The angular distributions for these particles are presented in Fig. 16.

The angular distribution for  $\gamma$  quanta from the  $\phi \rightarrow \eta\gamma$  decay is described with the formula:  $\frac{1+\cos^2\theta}{2}$ .

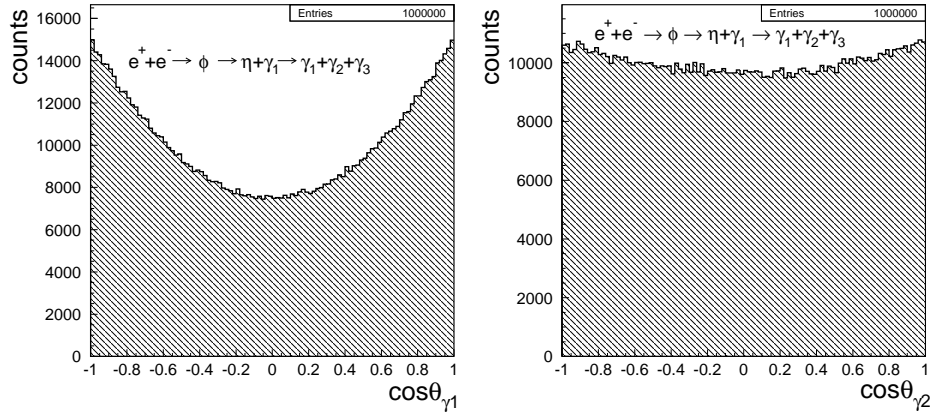


Figure 16: Simulated angular distributions for photons from reaction:  $e^+e^- \rightarrow \phi \rightarrow \eta \gamma \rightarrow 3\gamma$ .

Interestingly, Fig. 16 indicates that also  $\gamma$  quanta from subsequent  $\eta$  meson decay have still small contribution in the form of  $\cos^2\theta$ .

The decrease along the module of the solid angle as seen from the interaction point is shown in Fig. 17.

The variation of the solid angle decrease the events population towards the edges. The third effect which play a role in this context is the angle at which particle hits the detector surface and hence the angle of the shower propagation (see Fig. 18).

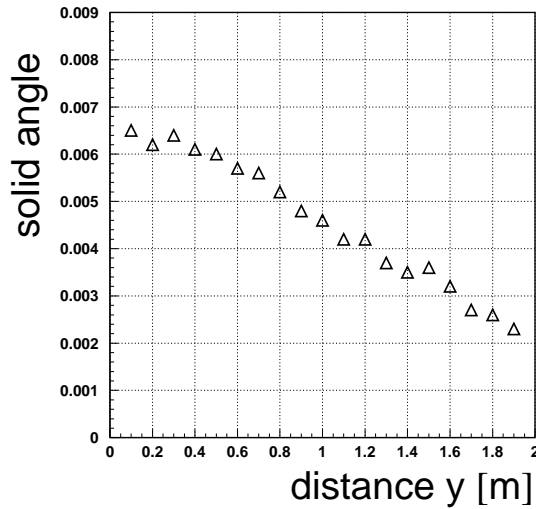


Figure 17: The solid angle distribution as a function of the distance from the center of the module.

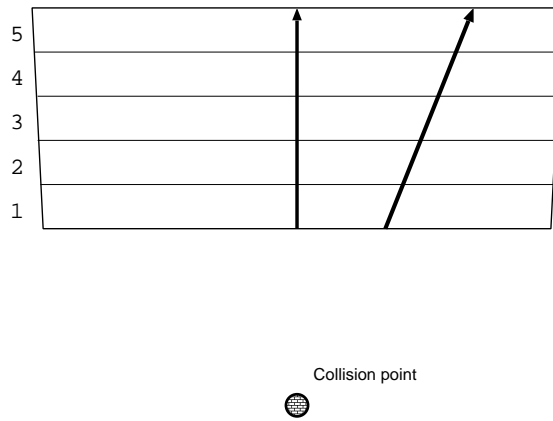


Figure 18: Schematic view of the particle tracks for two different entering examples.

Due to this fact in the first layer the energy deposited by showers in the middle of the module is lower than on the sides. Therefore, in subsequent layers relatively larger fraction of the energy of the shower will be deposited in the middle of the module and less on its sides. Hence, the shapes of distributions observed in Fig. 15 is determined by three discussed effects: angular distribution of  $\gamma$  quanta, changes of the solid angle, and variation of the fractional length of the showers in the layers as a function of the impact angle.

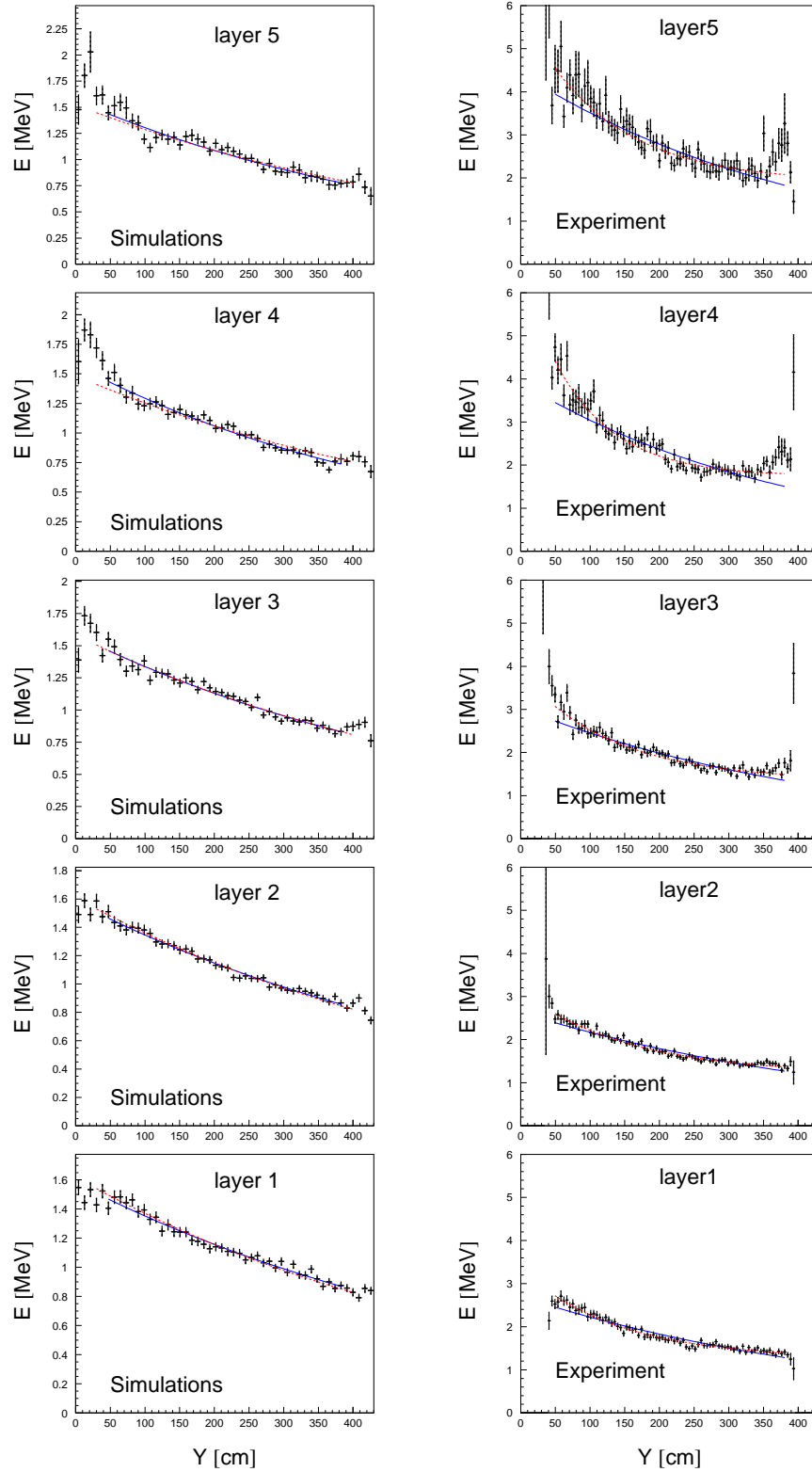


Figure 19: The energy distributions as seen at one side of the module: Monte Carlo (left column) and experimental data (right column). The curves are described in the text. Courtesy of Eryk Czerwiński and B. Di Micco [54].

In order to achieve a uniform, energy deposition along the module a simulated energy deposit distributions (Fig. 15) were fit with second order polynominal functions which were then used to normalize the experimental spectra and for the check also simulated spectra were normalized in the same way. Fig. 19 presents an energy of signals registered at one side of the module as a function of the distance between the edge of the module and the hit position. In order to establish a value of the light attenuation length ( $\lambda$ ) we fit to the spectra from Fig. 19 (right column) an exponential function:

$$E(y) = \alpha \cdot e^{-\frac{y}{\lambda}}, \quad (8)$$

with  $\alpha$  and  $\lambda$  being a free parameters [54]. The result of the fit is shown as dark blue, continuous line in Fig. 19 (right column). The weighted averages of attenuation length determined at both sides (A and B) amounts to  $522 \pm 7$  cm and  $407 \pm 9$  cm, for 1,2,3 layers and for 4,5 layers, respectively. The result is shown as a red, dashed curve in Fig. 19 (right).

As a next step the determined attenuation length were used to simulate the light output at the edges of the module with the DIGICLU program. The result is shown in Fig. 19 (left). These studies were made to check if results from simulations are in agreement with results which were achieved from the experimental data sample. The code of the lines is the same as in the right panel. The simulated and experimental spectra are in very good agreement except a region below 50 cm and above 400 cm. This is due to the fact that this part of the barrel is situated behind the endcap modules. And in the simulations presented in this thesis only a barrel part of the calorimeter is taken into account. Furthermore we tested also a fit with a function with two attenuations lengths [34]:

$$E(z) = \alpha_1 \cdot e^{-\frac{z}{\lambda_1}} + \alpha_2 \cdot e^{-\frac{z}{\lambda_2}}. \quad (9)$$

The result is presented in Fig. 19 where left column indicates results from simulations and right column shows experimental data. As one can see both presented fits describe the data well.

#### 4.2.2 Parametrization of the energy threshold function

In the experiment the signals which amplitude is lower than a given threshold are not read by the TDC board and information about their times is missing. In order to account for this effect in simulations the threshold curve was determined using the ratio between the number of cells with time information over all cells as a function of the cell energy. This ratio is shown in Fig. 20.

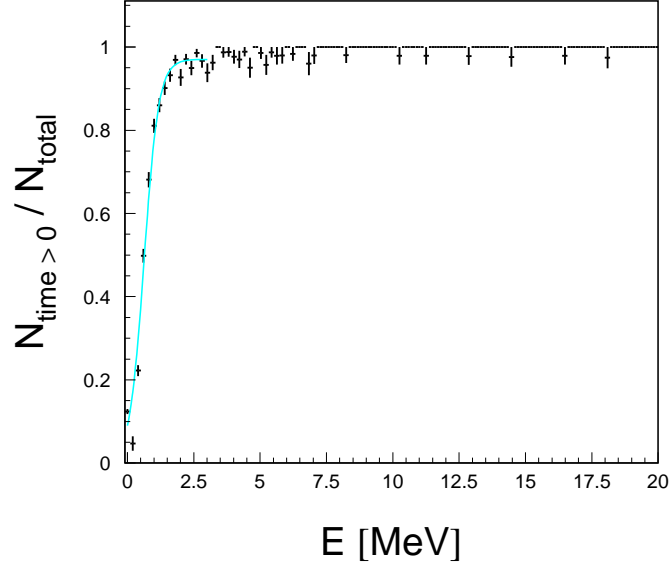


Figure 20: Ratio of number of cells with both time and energy signal to total number of cells with an energy signal. Courtesy of E. Czerwiński and B. Di Micco [54].

One can see that the distribution is not a step-like function but rather a smooth increase of the ratio in the range from 0 to 2 MeV is observed. The shape of this increase can be described by the Fermi-Dirac distribution [55,52,?]:

$$f_{th}(E) = (1 + e^{-\frac{E-\mu}{\sigma}})^{-1}, \quad (10)$$

with free parameters  $\mu$  and  $\sigma$ . A fit for the range of energy near the threshold resulted in the following values:

$$\begin{aligned} \sigma &= 0.2644 \pm 0.0068 \text{ MeV}, \\ \mu &= 0.5648 \pm 0.0087 \text{ MeV}. \end{aligned}$$

#### 4.2.3 Calibration of the ionization deposits

The next step in the tuning of the simulation program is the adjustment of the absolute scale of the energetic response of the calorimeter. For this purpose we compared results of simulations with experimental distribution of energy deposits in the calorimeter module. The results for five layers are shown in Fig. 21 (left column).

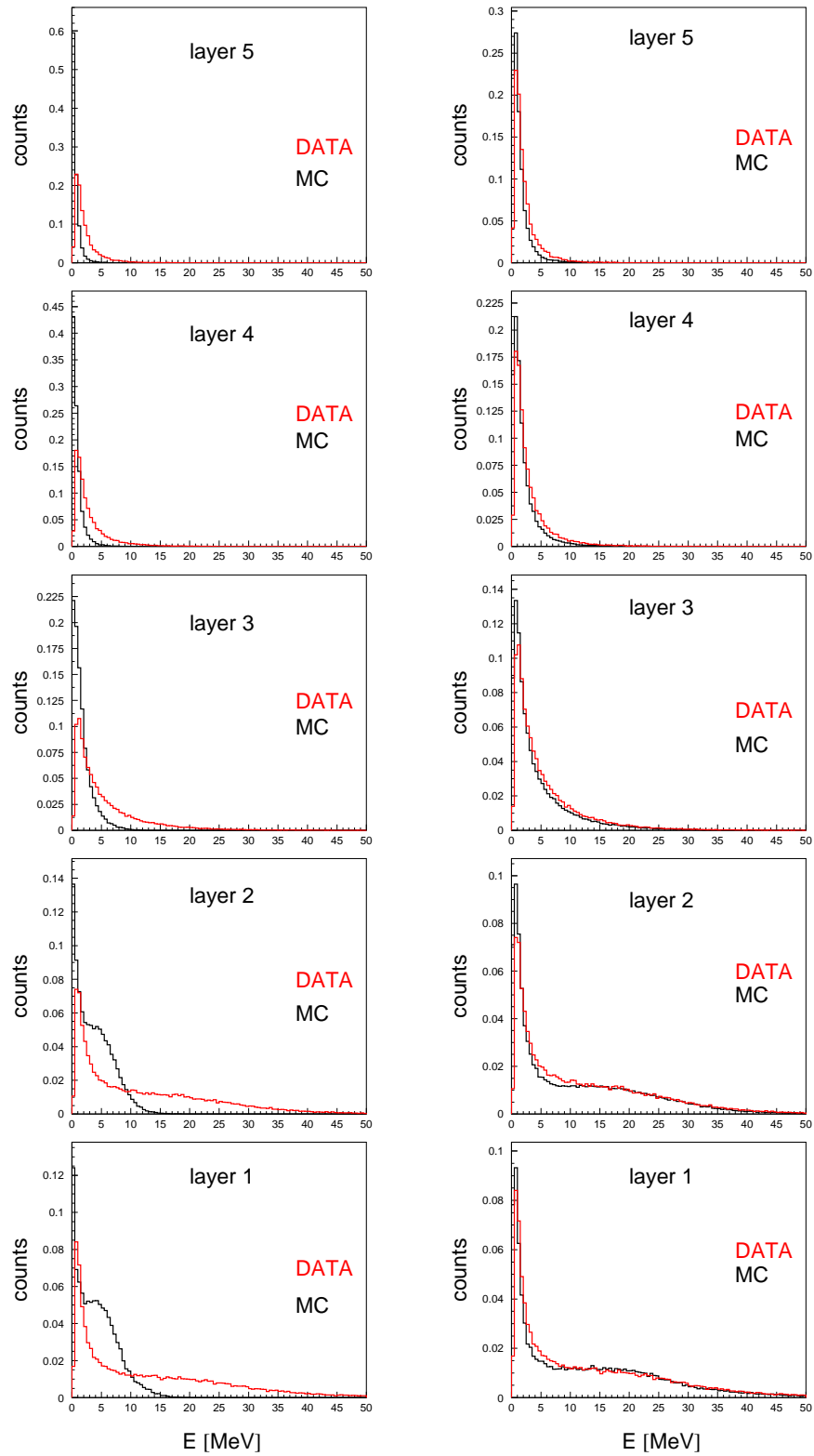


Figure 21: Comparison of energy deposits in 5 layers as determined from simulation (black line) and experiment (red line). The presented results before (left column) and after (right column) calibration. Courtesy of E. Czerwiński and B. Di Micco [54].

One sees that the energy deposits reconstructed for simulated events are much smaller than for the experimental data. In order to correct this discrepancy, the simulated values of energy deposits were multiplied by the factor of 3.74. The shape of the corrected spectra is in a very good agreement with experimental distributions for each layer (Fig. 21 right).

Next, correction was needed because the clustering algorithm not always is able to reconstruct the entire energy deposited in the clusters. That's why sum of energy deposits which were simulated is greater than sum of energy in reconstructed clusters. For this case a linearity correction was needed and it was obtained with requiring straight line with slope 1 (blue line in Fig. 22).

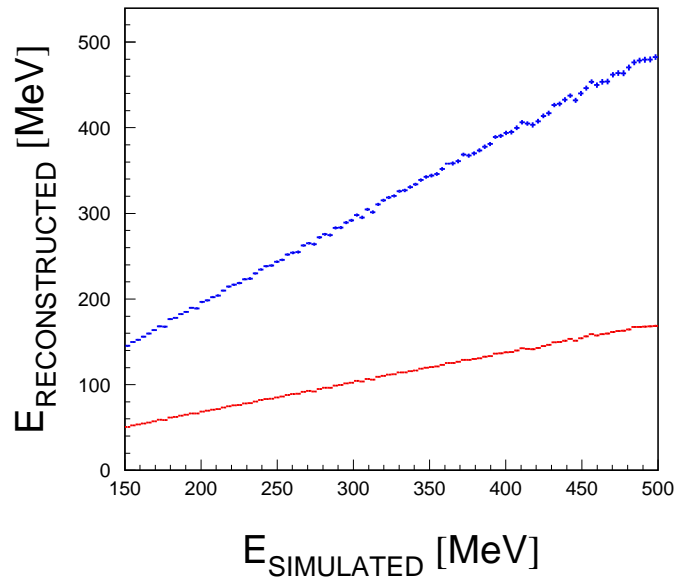


Figure 22: Calibration of the simulated and reconstructed energy. Courtesy of E. Czerwiński and B. Di Micco [54].

The red curve represents the situation before calibration (slope parameter is not equal 1) and blue after. Applying the corrections described in this section we achieved very good agreement between data and simulations of energy response of the calorimeter when using FLUKA and DIGICLU procedures [54].

## 5 Estimations of background due to the merging and splitting of photon clusters

The main motivation of this work is the estimation of merging and splitting effects for reactions like e.g.  $\eta \rightarrow 3\pi^0$  or  $K_S \rightarrow 2\pi^0$  which may constitute background in studies of the  $\eta \rightarrow \pi^0\gamma\gamma$  and  $K_S \rightarrow 3\pi^0$  reactions, respectively. In Table 5 we present a Branching Ratios (BR) for the main investigated reactions and for the background channels.

Table 5: Branching Ratios for examples of studied reactions and the background decays [59].

Main Decay	BR (%)	Background Channel	BR (%)	Effect
$\eta \rightarrow \pi^0\gamma\gamma$	$(4.4 \pm 1.6) \cdot 10^{-6}$	$\eta \rightarrow 3\pi^0$	$(32.51 \pm 0.28)$	merging
$K_S \rightarrow 3\pi^0$	$< 1.2 \cdot 10^{-9}$	$K_S \rightarrow 2\pi^0$	$(30.69 \pm 0.05)$	splitting
$K_L \rightarrow 2\pi^0$	$(8.69 \pm 0.04) \cdot 10^{-2}$	$K_L \rightarrow 3\pi^0$	$(19.56 \pm 0.14)$	merging

In this Table one can see that all the background reactions have much bigger BR (many orders of magnitude) than the investigated channels. Therefore, even small merging and splitting effects may obscure considerably observation of signals from  $\eta \rightarrow \pi^0\gamma\gamma$ ,  $K_S \rightarrow 3\pi^0$  or  $K_L \rightarrow 2\pi^0$  decays.

### 5.1 Merging of clusters from $\eta \rightarrow 3\pi^0$ as a background for the $\eta \rightarrow \pi^0\gamma\gamma$ channel

The example of the merging effect, inducing a wrong cluster counting, comes from analysis of the  $\eta \rightarrow \pi^0\gamma\gamma$  events [6]. The Branching Ratio (BR) for  $\eta \rightarrow 3\pi^0$  is by several orders of magnitude more frequent than  $\eta \rightarrow \pi^0\gamma\gamma$  (see Table 5).

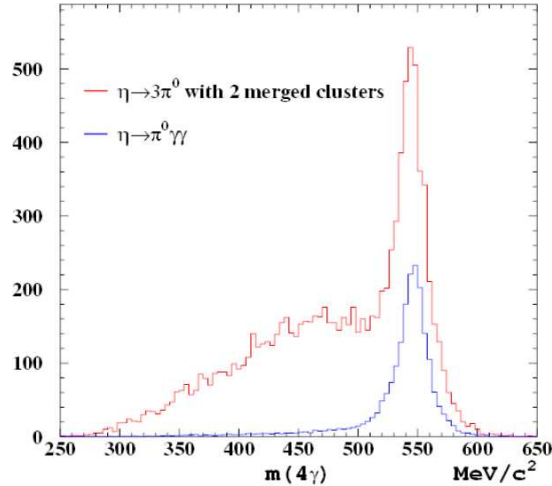


Figure 23: Invariant mass of four photons for the  $\eta \rightarrow \pi^0\gamma\gamma$  events and for the  $\eta \rightarrow 3\pi^0$  background with two merged clusters [6].

In Fig. 23 a consequence of the merging of clusters is presented for the case when 6 $\gamma$  quanta from 3 $\pi^0$  decay were reconstructed as 4 clusters. In this case the topology of  $\eta \rightarrow 3\pi^0$  becomes equal to that of the  $\eta \rightarrow \pi^0\gamma\gamma$  reaction. And as a result on 4 $\gamma$  invariant mass distribution one can see a big peak from background channel exactly at the mass of the  $\eta$  meson [3].

The next very interesting example of reactions for which problems with merging of clusters is significant and which can be studied with the KLOE calorimeter [11] is CP violating decay  $K_L \rightarrow 2\pi^0$ . An example of such event is presented in Fig. 24.

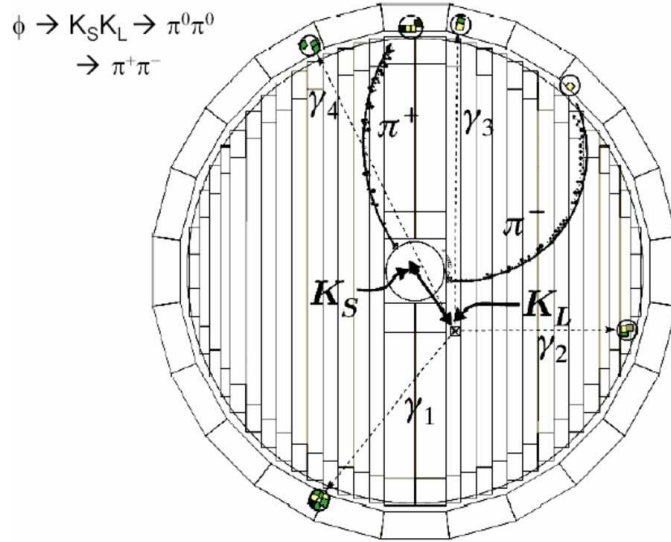


Figure 24: A CP-violating  $\phi \rightarrow K_S K_L$  event. The  $K_S$  decays into  $\pi^+ \pi^-$  very close to the interaction point. The  $K_L$  decays into  $\pi^0 \pi^0$  further away resulting in four photons which are detected by the calorimeter [11].

The  $K_S$  meson decays into  $\pi^+ \pi^-$  near the collision point. The  $K_L$  meson decays into  $\pi^0 \pi^0$  and then these pions decaying through electromagnetic interaction to 4 $\gamma$  quanta. Those four photons are detected by the EmC. Thus  $K_L \rightarrow 3\pi^0 \rightarrow 6\gamma$  with two merged clusters may obscure a signal from the  $K_L \rightarrow 2\pi^0$  reaction.

Implementation of the full barrel geometry into the FLUKA program allowed us to study the effect of merging and splitting quantitatively. And hereafter we will present the results for the reconstruction of clusters from the  $\eta \rightarrow 3\pi^0$  and  $K_S \rightarrow 2\pi^0$  in view of the merging and splitting which estimation is crucial for the study of the  $\eta \rightarrow \pi^0\gamma\gamma$  and  $K_S \rightarrow 3\pi^0$  decays.

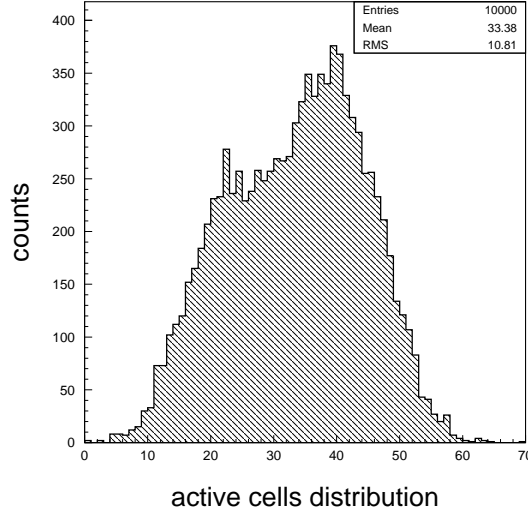


Figure 25: Distribution of the number of active cells for reaction:  $e^+e^- \rightarrow \phi \rightarrow \eta\gamma \rightarrow 3\pi^0\gamma \rightarrow 7\gamma$ . Statistics is equal to 10 000 events.

The Fig. 25 shows a distribution of the total number of cells which given signal. Whereas distribution of the total number of preclusters and the total number of reconstructed clusters are presented in the next Figure.

The reconstruction possibilities of the clustering algorithm are presented in Fig. 26.

One can see that the most probably the clustering algorithm reconstructs 5 or 6 clusters even though 7 photons had hit the detector.

The frequencies of reconstructed clusters are presented in Table 6. One can see that the topology of this channel could be interpreted both with 4  $\gamma$  quanta (15.13%) as well as with 6 photons (23.26%). In the first case this channel could constitute a background for  $\eta \rightarrow \pi^0\gamma\gamma$  reaction (merging effect).

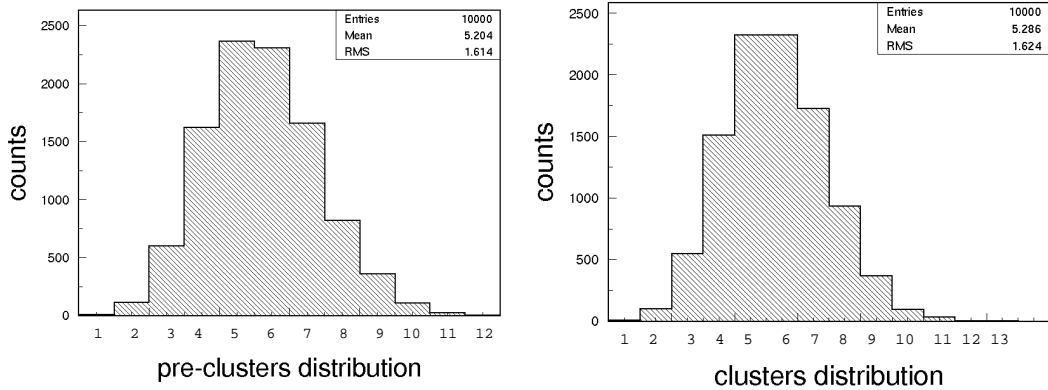


Figure 26: Distributions of the reconstructed pre-clusters (left) and total reconstructed clusters (right), for reaction:  $e^+e^- \rightarrow \phi \rightarrow \eta\gamma \rightarrow 3\pi^0\gamma \rightarrow 7\gamma$ . Statistics is equal to 10 000 events.

Table 6: Efficiency of the reconstructed pre-clusters and clusters for  $e^+e^- \rightarrow \phi \rightarrow \eta\gamma \rightarrow 3\pi^0\gamma \rightarrow 7\gamma$  channel. Statistics equal to 10 000 events.

Number of reconstructed preclusters and clusters	Frequency for preclusters (%)	Frequency for clusters (%)
1	0.12	0.12
2	1.11	1.02
3	5.99	5.50
4	16.22	15.13
5	23.70	23.23
6	23.09	23.26
7	16.60	17.27
8	8.25	9.35
9	3.59	3.71
10	1.06	0.97
11	0.22	0.36
12	0.27	0.05
13	0.00	0.03

## 5.2 Splitting of clusters for $K_S \rightarrow 2\pi^0$ as a background for $K_S \rightarrow 3\pi^0$

Splitting is related with the features of the EmC detector and with reconstruction possibilities of the KLOE clustering algorithm which not always correctly reconstructs positions and energies of particles interacting with detector material and may assign more than one cluster to signals induced by a single particle.

Fig. 27 shows that data with  $6\gamma$  quanta in the final state gives in most cases much

lower  $\chi^2$  when fit under the hypothesis of  $2\pi^0$  then for the  $3\pi^0$  hypothesis whereas for a real  $6\gamma$  events originating from the  $K_S \rightarrow 3\pi^0$  decay one expects  $\chi_{3\pi}^2$  to be small and  $\chi_{2\pi}^2$  to be large as it is seen in the sample of the MC  $K_S \rightarrow 3\pi^0$  data (Fig. 27).

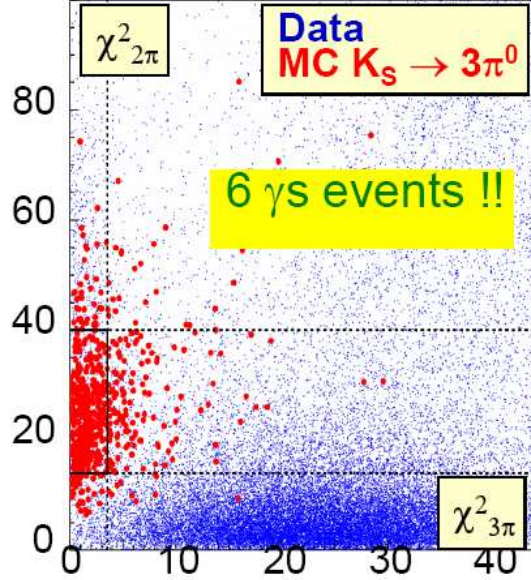


Figure 27: Distribution of the  $\chi^2$  variable determined under  $3\pi^0$  and  $2\pi^0$  hypotheses of the MC  $K_S \rightarrow 3\pi^0$  signal and of the data [3].

Therefore, the  $K_S \rightarrow 2\pi^0 \rightarrow 4\gamma$  decay with two splitted clusters gives the same event topology as expected for the  $K_S \rightarrow 3\pi^0 \rightarrow 6\gamma$  reaction.

We investigated  $e^+e^- \rightarrow \phi \rightarrow K_L K_S \rightarrow K_L 2\pi^0 \rightarrow K_L 4\gamma$  reaction with condition that all four  $\gamma$  quanta hit the barrel calorimeter. We performed approximation that  $K_S$  meson decays exactly in the collision point. However, we suppose that this approximation hasn't significant influence on the results because a distance between collision point and hit position at calorimeter surface is at least 2 meters. We present the distribution of the active cells in Fig. 28.

We also investigated the distribution of pre-clusters and clusters for this channel (Fig. 29). One can see that in 18.08% a clustering algorithm reconstructed  $6\gamma$  quanta. Therefore for this case the topology of investigated channel with 6 reconstructed photons (two splitted clusters) is the same as for  $K_S \rightarrow 3\pi^0$  reaction and it constitute a background for this decay. The fractions of numbers of reconstructed clusters are presented in the Tab. 7.

One can see that correct reconstruction of four clusters constitutes only about 26% of total number of events. Both merging and splitting effects could be reduced by the better shower shape reconstruction induced by a finer read-out granularity.

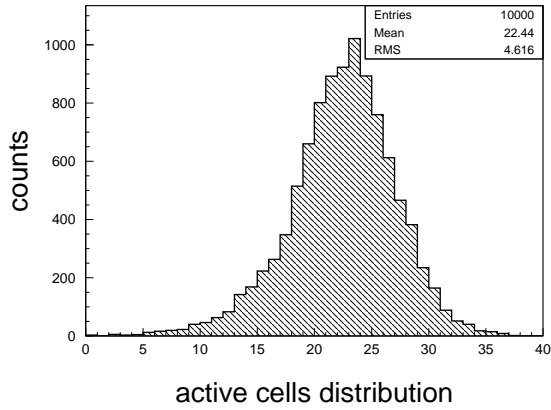


Figure 28: Distribution of the number of active cells for  $e^+e^- \rightarrow \phi \rightarrow K_L K_S \rightarrow K_L 2\pi^0 \rightarrow K_L 4\gamma$  reaction. Statistics is equal to 10000 events.

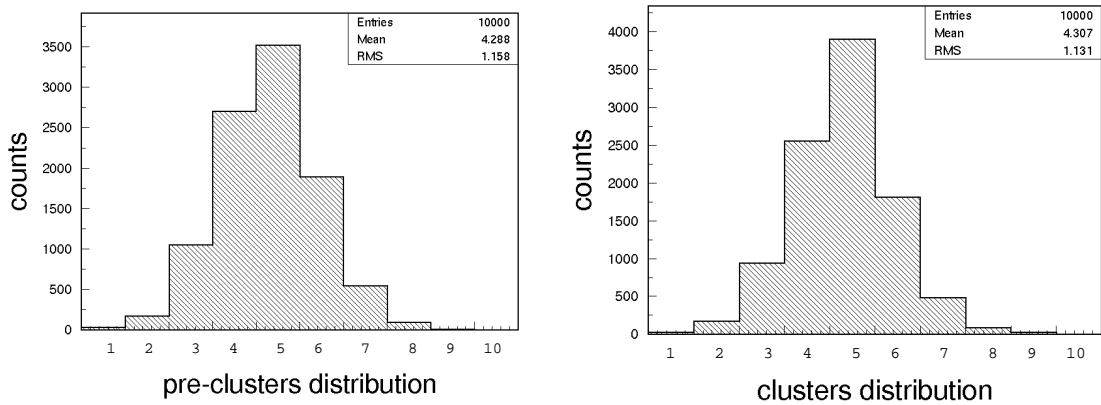


Figure 29: Distributions of the number of reconstructed pre-clusters (left panel) and total number of reconstructed clusters (right panel), for  $e^+e^- \rightarrow \phi \rightarrow K_L K_S \rightarrow K_L 2\pi^0 \rightarrow K_L 4\gamma$  reaction. Statistics is equal to 10000 events.

But also the identification of particles based on the shower shape analysis would greatly take advantage of an increase in the calorimeter granularity [3].

Table 7: Efficiency of the reconstructed pre-clusters and clusters for  $e^+e^- \rightarrow \phi \rightarrow K_L K_S \rightarrow K_L 2\pi^0 \rightarrow K_L 4\gamma$  channel.

Number of reconstructed preclusters and clusters	Frequency for preclusters (%)	Frequency for clusters (%)
1	0.26	0.26
2	1.70	1.72
3	10.47	9.38
4	26.97	25.59
5	35.23	39.05
6	18.94	18.08
7	5.42	4.84
8	0.94	0.86
9	0.06	0.21
10	0.01	0.01

### 5.3 Reconstruction efficiency with the KLOE clustering algorithm

In order to estimate the reconstruction efficiency of the present KLOE clustering algorithm we investigated detector response for two  $\gamma$  quanta with momentum of 500 MeV/c. The response was generated as a function of the distance between the  $\gamma$  quanta. Subsequently we have reconstructed a total number of clusters which were recognized by clustering algorithm. The two investigated situations are shown in Fig. 30 and in Fig. 31. In the first case the distance between photons on x axis is 0 cm and the distance on y axis was varied between 0 and 200 cm.

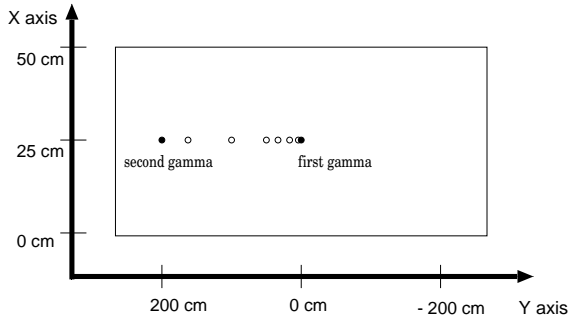


Figure 30: Hit positions of  $\gamma$  quanta for  $\Delta X = 0$  cm.

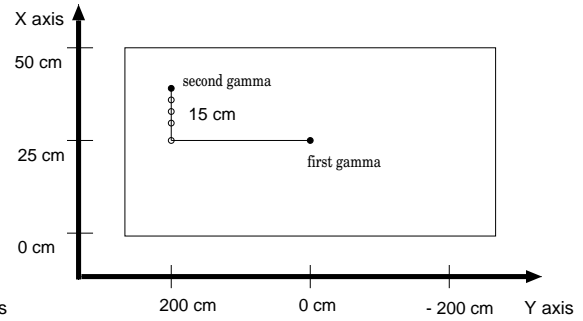


Figure 31: Hit positions of  $\gamma$  quanta for  $\Delta Y = 200$  cm.

If the reconstruction efficiency of the KLOE algorithm was 100%, this algorithm would always reconstruct two clusters which we interpret as two photons which hit the module.

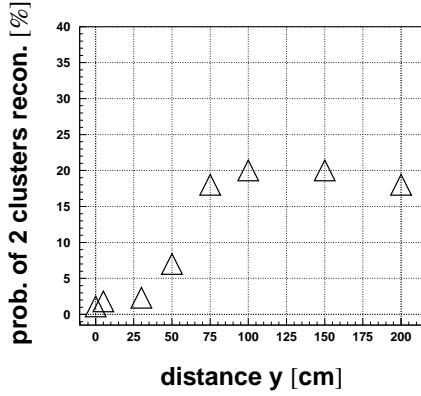


Figure 32: The efficiency of the two clusters reconstruction as a function of the distance along y axis provided that x coordinate for both photons was the same.

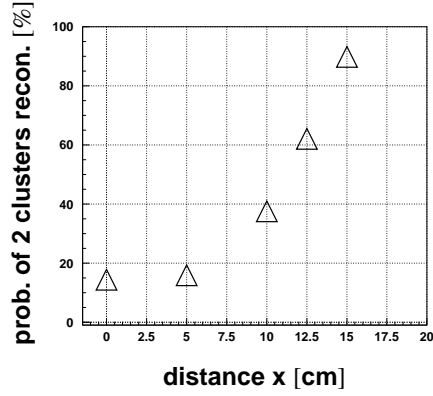


Figure 33: The efficiency of the two clusters reconstruction as function of the distance between photons along the x axis.

But results of simulations show (see Fig. 33 and Fig. 32) that reconstruction efficiency is changing as a function of distance between these two particles.

As expected the reconstruction efficiency is increasing with increasing distance between two  $\gamma$  quanta. This result shows that the biggest problem with reconstruction is in the case when particles hit with the small difference in the x coordinate.

#### 5.4 Reconstruction efficiency as a function of the photocathode quantum efficiency

We have performed investigations of the influence of the quantum efficiency of the photocathode on the merging and splitting effects. We carried out our simulations using a vertex generator for reactions:  $e^+e^- \rightarrow \phi \rightarrow \eta\gamma \rightarrow 3\gamma$  and  $e^+e^- \rightarrow \phi \rightarrow \pi^0\gamma \rightarrow 3\gamma$ . Then we simulated the calorimeter response using FLUKA program, reconstructed PM response by means of the DIGICLU procedure and finally reconstructed clusters by means of the present KLOE clusterisation algorithm. The studies presented in this section were performed for one module only. The efficiency is defined by the following formula:

$$\epsilon = \frac{N(\geq 1cluster)}{N(\geq 1hit)}, \quad (11)$$

where: N is the total number of events with a condition in parenthesis. This condition assures that we take events for which the module was hit by at least one  $\gamma$ .

The results of simulations for the single calorimeter module are shown in Fig. 34.

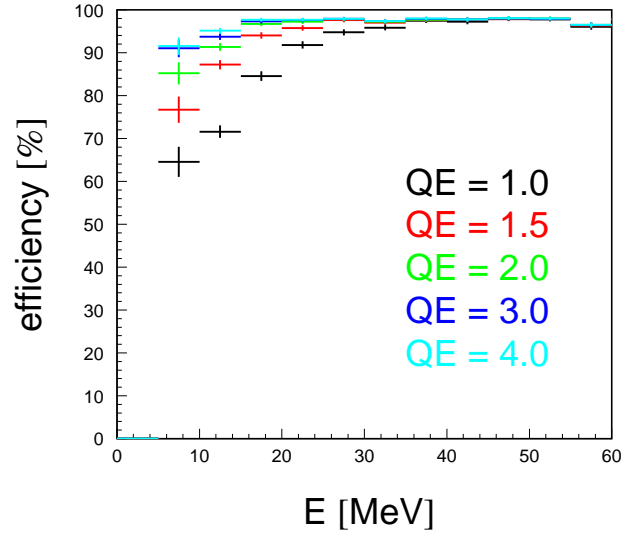


Figure 34: Reconstruction efficiency as a function of the energy and quantum efficiency. Courtesy of E. Czerwiński [51].

We have studied [54] the reconstruction efficiency as a function of the energy in the cluster for five values of the quantum efficiency as depicted inside the Figure. QE = 1 represents results for a present quantum efficiency of photomultipliers used at KLOE, amounting to 23% [51,60]. Remaining values of QE indicates a factors by which the efficiency was increased in our investigations. From these studies one can see that as expected with the increasing value of the quantum efficiency for photomultipliers the efficiency of reconstruction is increasing too.

### 5.5 Merging and splitting probabilities as a function of the quantum efficiency

Subsequently, we determined the influence of value of the quantum efficiency on the magnitude of the merging and splitting effects. The results of these simulations are shown in Fig. 35.

The merging probability was defined according to the following formula:

$$\text{merg. probability} = \frac{N(1 \text{ cluster and } \geq 2 \text{ hits})}{N(\geq 1 \text{ cluster and } \geq 2 \text{ hits})} \quad (12)$$

and the splitting probability was defined as:

$$\text{split. probability} = \frac{N(\geq 2 \text{ clusters and } 1 \text{ hits})}{N(\geq 1 \text{ cluster and } 1 \text{ hits})} \quad (13)$$

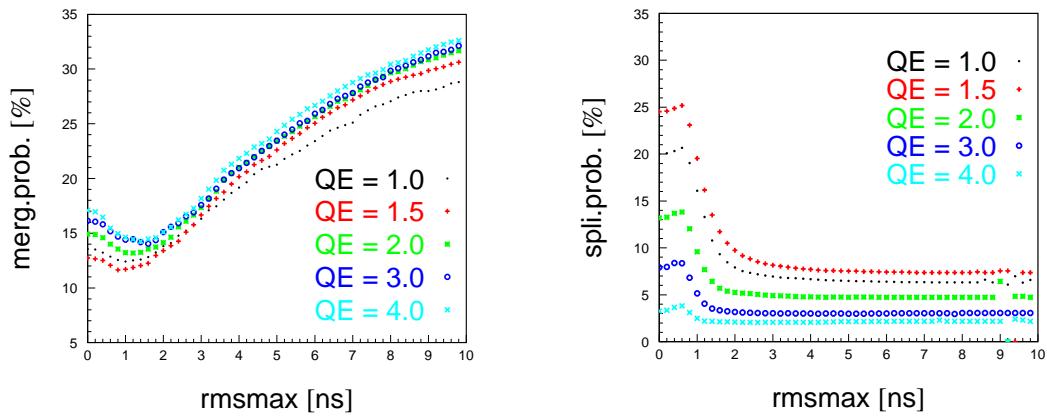


Figure 35: Merging and splitting studies with single EmC module. Rmsmax is a value of the width (RMS) of the time distribution of the cells above which the clustering algorithm tries to break a cluster [54]. At present KLOE algorithm this value is equal to 2.5 ns. Courtesy of E. Czerwiński [51].

Fig. 35 shows that the splitting probability increase with increasing of the quantum efficiency of photomultipliers [54] but one can see that merging effect is much less sensitive to the changing of the quantum efficiency.

## 6 Conclusions

We have built a full simulation of the Barrel Calorimeter of the KLOE detector with FLUKA Monte Carlo package. This implementation of the geometry was used for simulations of the physical energy response of the calorimeter. The Monte Carlo cooperates with vertex generator which reproduces kinematics of the physical reactions.

We estimated influence of merging and splitting of clusters for reconstruction possibilities of the particles on the whole barrel calorimeter with a present clustering algorithm. In particular we estimated these effects as a function of the quantum efficiency of photomultipliers [54]. As a results we found that increase of the quantum efficiency does not improve significantly the cluster reconstruction in view of merging and splitting effects.

The prepared program with geometry of the 24 modules of the barrel calorimeter enables fast simulations of a choosen reaction channel and facilitates studies of the detector response to different reactions separately.

This geometry may be used to test response of photomultipliers with higher granularity of cells, especially for testing performances of the multianode photomultiplier.

Implemented geometry of the barrel calorimeter in FLUKA reproduces the merging and the splitting effects, and permits also to study the efficiency of clusterisation algorithm at the edges of the modules in the barrel calorimeter. These all usefull options come out from the fact that the smallest parts of detector (the fibers structure) were realistically implemented in FLUKA Monte Carlo.

We investigated a shapes of peaks for time distribution of reconstruction of clusters, the shapes are changing as a function of distance between photons. This information could be very useful for the upgrade of the clustering algorithm [61].

We estimated also the influence of merging and splitting of clusters for  $e^+e^- \rightarrow \phi \rightarrow K_L K_S \rightarrow K_L 2\pi^0 \rightarrow K_L 4\gamma$  and  $e^+e^- \rightarrow \phi \rightarrow \eta\gamma \rightarrow 3\pi^0\gamma \rightarrow 7\gamma$  reactions. The studies were made determining the response of the whole barrel calorimeter with DIGI-CLU program.

Finally, it is worth mentioning that our study encouraged the authors of the FLUKA to upgrade the program and in the near future a new version permitting to replicate the cells more than once will be available.

## A Kinematic fit procedure

The kinematic fit procedure is used to correct measured quantities  $x_i$  ( $x_1 \dots x_i \dots x_n$ ) in case of redundancy in the measured set of variables. In most cases  $x_i$  is normal distributed around  $x_i^{true}$  with standard deviation  $\sigma_i$ .

$$\sigma(x_i) = \frac{1}{N-1} \sum_i^N (x_i - \bar{x})^2 \quad (14)$$

$$(15)$$

where  $\bar{x}$  is a average of the all  $x_i$  values. Variables  $x_i^{true}$  could be constrained by some physical law (in our investigations by energy and momentum conservation) in this case they must satisfy  $k$  equations, which can in general be written in the form:

$$F_j(x_1^{true}, \dots, x_n^{true}) = 0 \quad j = 1, \dots, k \quad (16)$$

The main purpose of using fit procedure is to find a new approximation ( $\mu_i$ ) of  $x_i^{true}$  value by minimizing the quantity:

$$\chi^2 = \sum_i \frac{(x_i - \mu_i)^2}{\sigma_i^2} \quad (17)$$

and imposing the (16) constraints on  $\mu_i$ . This purpose can be achieved using langrangian multipliers method, that consists of minimizing the quantity:

$$\chi^2 = \sum_i \frac{(x_i - \mu_i)^2}{\sigma_i^2} + \sum_j \lambda_j F_j(\mu_1, \dots, \mu_n) \quad (18)$$

related with the variables  $\mu_i$  and  $\lambda_j$  [6]. To minimize a  $\chi^2$  value an iterative procedure is needed to be used.

The detailed description of the  $\chi^2$  distribution can be found e.g. in [56].

## B Monte Carlo Methods

Monte Carlo simulations are methods of solving numerical assignments with the aid of adequate constructed statistical computations. They are frequently used in experimental and theoretical physic [57]. Although computer memory and processor performance have increased dramatically over the last two decades, many physical problems are too complicated to be solved without approximations of the physics processes, quite apart from the approximations inherent in any numerical method. Therefore, most calculations done in computational physics involve some degree of approximation [58].

Solving a physical problem often requires to solve an ordinary or partial differential

equation. This is the case in for example classical mechanics, electrodynamics, quantum mechanics and fluid dynamics. On the other hand in statistical physics we must calculate sums or integrals over large numbers of degrees of freedom.

Whatever type of problem we try to solve, it is only in very few cases that analytical solutions are possible. In most cases we therefore resort to numerical calculations to obtain useful results [58].

These methods are used in physic for the last sixty years [57].

### C Energy distributions for $\gamma$ quanta

We have investigated<sup>6</sup> the distribution of the energy and the position of the  $\gamma$  quanta on the bottom surface of a single calorimeter module. We performed simulations for reactions:  $e^+e^- \rightarrow \phi \rightarrow \eta\gamma \rightarrow 3\gamma$  and  $e^+e^- \rightarrow \phi \rightarrow \eta\gamma \rightarrow 3\pi^0\gamma \rightarrow 7\gamma$ . The result is presented in Fig. 36 in upper and lower panel, respectively. In the left column in Fig. 36, one can see hit distributions for particles entering the module. In the right panels in this figure the sharp signals originate from a monenergetic  $\gamma$  quanta from  $\phi$  meson decay with energy equal to 363 MeV. In the case of the  $e^+e^- \rightarrow \phi \rightarrow \eta\gamma \rightarrow 3\pi^0\gamma \rightarrow 7\gamma$  reaction we observe more events at the lower energy range. These signals originate from  $\gamma$  quanta from  $\pi^0$  meson decays. As a further example in Fig. 37 we present energy spectra separately for the radiative photon and for the photon from the  $\eta$  and pion decays.

In the left panel the monoenergetic signal for photon from  $\phi$  meson decay is shown. The middle panel presents energy distribution for photons from the  $\eta$  meson decay and the third panel presents the energy distribution for  $\gamma$  quanta from  $\pi^0$  mesons decays.

---

<sup>6</sup>We used the BXDRAW subroutine in this investigations [32].

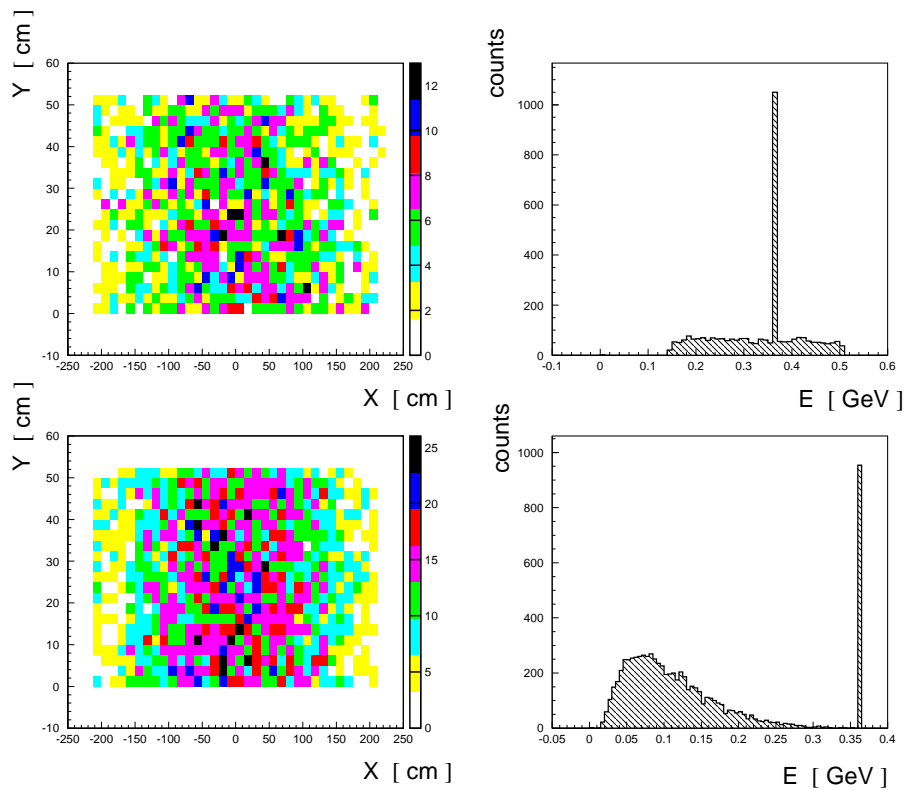


Figure 36: Simulated distributions of the hit position at the surface of one calorimeter module (left panel) and energy spectra (right panel) of  $\gamma$  quanta from the reactions  $e^+e^- \rightarrow \phi \rightarrow \eta\gamma \rightarrow 3\gamma$  (upper panel) and  $e^+e^- \rightarrow \phi \rightarrow \eta\gamma \rightarrow 3\pi^0\gamma \rightarrow 7\gamma$  (lower panel).

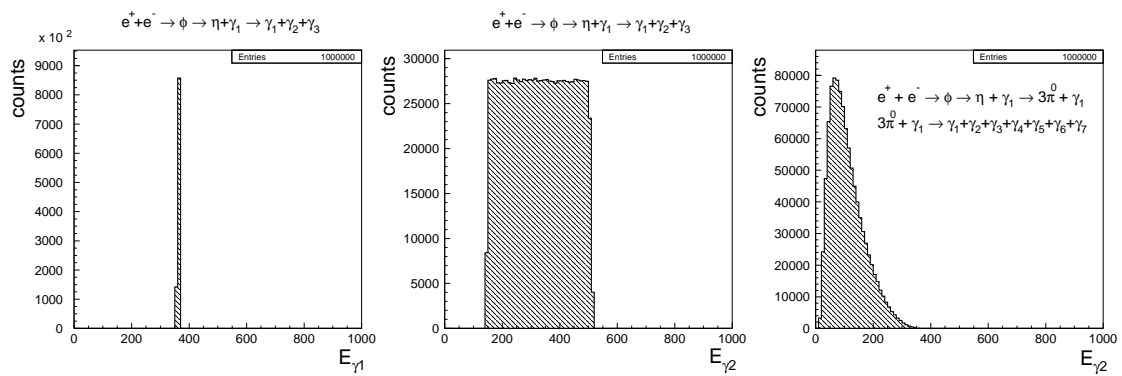


Figure 37: The energy distribution for photons from reactions:  $e^+e^- \rightarrow \phi \rightarrow \eta\gamma \rightarrow 3\gamma$  and  $e^+e^- \rightarrow \phi \rightarrow \eta\gamma \rightarrow 3\pi^0\gamma \rightarrow 7\gamma$ .

## D Time distribution for single and multi-gamma hits

In this appendix we investigated distributions of the sum and difference of times of light signals from the sides of the module. Our studies show that distributions are changing as a function of the distance between  $\gamma$  quanta hitting the module. This information could be used to improve efficiency of the KLOE clustering algorithm in the near future [61]. In Fig. 38 result for the situation where one  $\gamma$  quanta hit in the middle of the calorimeter module is presented. One can see only one peak for both difference and sum of time of signals from sides A and B.

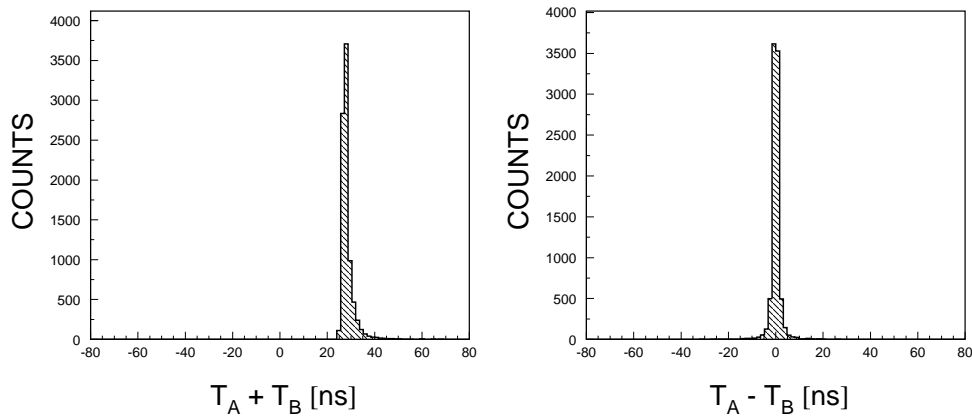


Figure 38: Distribution of sum and difference of time for one  $\gamma$  quanta.  $T_A$  and  $T_B$  denote the time where a signal from scintillating fibers comes into a photomultipliers on side A and side B, respectively.

For the two  $\gamma$  quanta which hit the surface<sup>7</sup> at the same x but different y the result is different (see Fig. 39). One can see that distribution of difference of times for signals from side A and B consists of three separated peaks and the distribution of the sum of times from sides A and B shows two maxima.

---

<sup>7</sup>Two studing cases of hit positions of photons entering the calorimeter surface are presented in Fig. 30 and Fig. 31. Positions of  $\gamma$  quanta are marked as black circles.

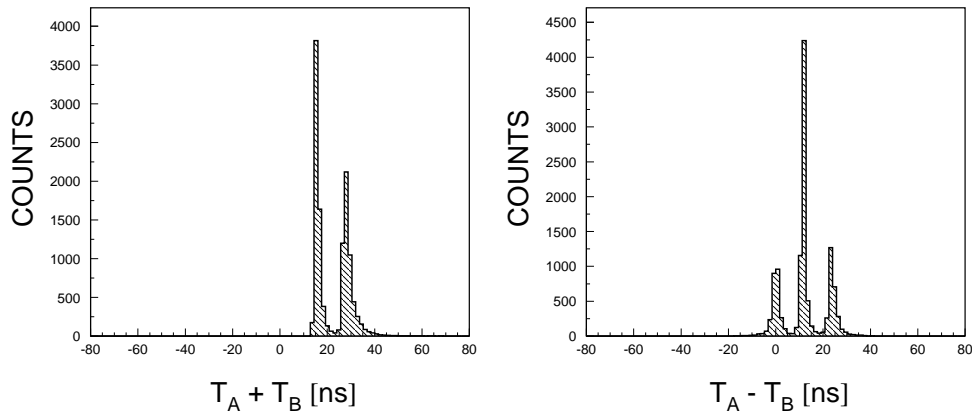


Figure 39: Distribution of sum and difference of time for two  $\gamma$  at the same x position but different y.

Next we investigated the situation where distance on x axis between two  $\gamma$  quanta is equal to 15 cm. In this case we observe only one maximum in the distribution of the sum and two maxima in the distribution of the difference of times (Fig. 40).

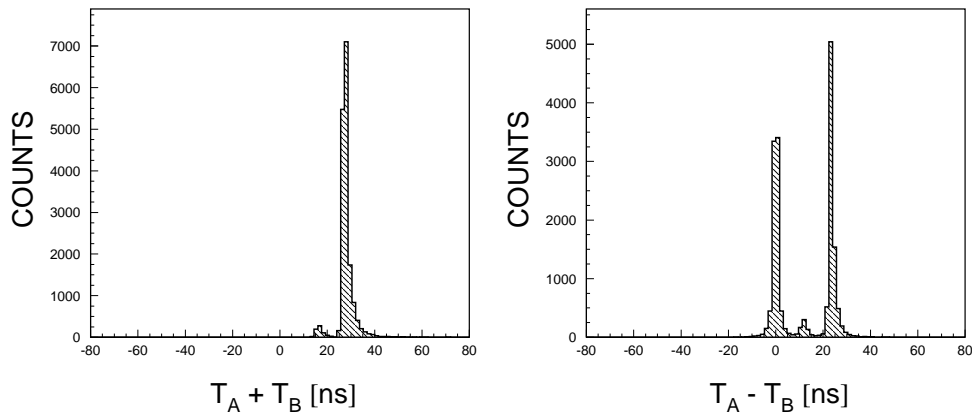


Figure 40: Distribution of sum and difference of time for two  $\gamma$  hitting the module with a distance of 15 cm along the x axis.

In the following we present an example of results of cell distributions simulated for several distances on x axis between places where photons hit the module and for several angle between a surface and a photon direction. The results of the sum of energy

deposited in cells for side A and B we present using a displayer program<sup>8</sup>. Fig. 41 presents a photomultipliers energetic response for one  $\gamma$  quanta which hit the middle of the module at an angle of 90 degrees.

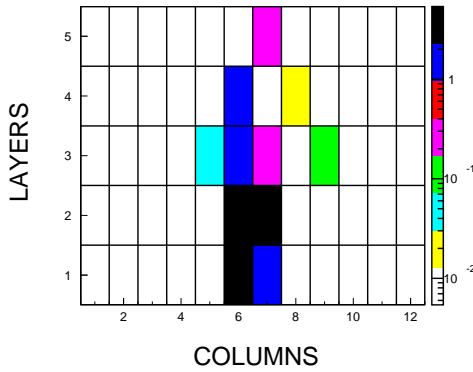


Figure 41: Distribution of cells for one  $\gamma$  quantum hitting with 90 degrees in the middle of the module.

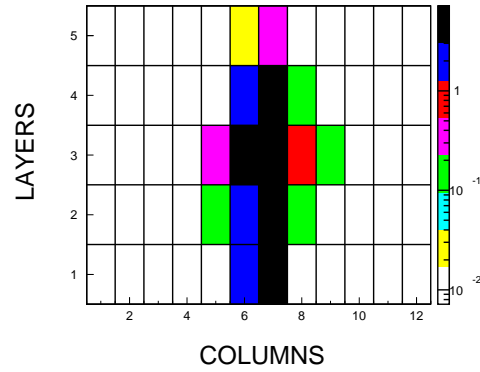


Figure 42: Distribution of cells for two  $\gamma$  quanta hitting with 90 degrees with a distance on y axis equal to 200 cm and with the same coordinate on x axis.

Comparing this result with the case (see Fig. 42) where two  $\gamma$  quanta hit the module at a distance on y axis equal to 200 cm but with the same x coordinate, we can see that it is not possible to distinguish these two situations due to the fact that the second case can be interpreted for example as one particle which hit the module but with higher energy. However, we can easily identify two particle events when a distance on the x axis between hit positions is larger than 15 cm (see also Fig. 33). In Fig. 44 a distribution for the case when the distance between two photons was equal to 25 cm is presented.

We simulated also a situation where photon hit the module with the angle equal to 30 degrees (see Fig. 43) with respect to the surface. One can see two cells on the right side on this plot which aren't connected to the main cluster. It is worth to mention that such distributions may be interpreted as two hits.

<sup>8</sup>This program written in a Fortran code [54] is based on the CERN library tool [62].

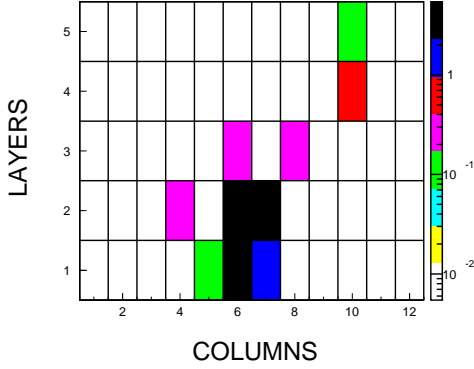


Figure 43: The distribution of cells for one  $\gamma$  quantum hitting the module with the angle equal to 30 degrees with respect to the surface.

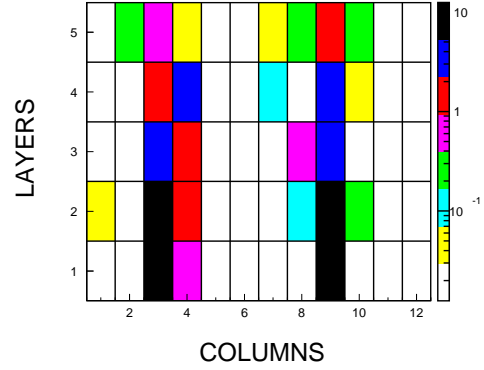


Figure 44: The distribution of cells for two  $\gamma$  quanta hitting the module with 25 cm distance along x axis.

## E Estimation of probability for multi-gamma hits at a single calorimeter module

Using FLUKA Monte Carlo with vertex generator we were able to estimate a probability on the multi-gamma hits at calorimeter module originating from the  $\eta$  meson decays. We estimated a multiplicity of the  $\gamma$  quanta on one module of the KLOE calorimeter. By multiplicity we define the number of  $\gamma$  quanta hitting one module (Fig. 45). If it is equal to zero, it signifies that our tested module did not see any  $\gamma$ , if it is equal to one then the module registered one gamma quantum. Due to the axial symmetry of KLOE this result is valid for all detection modules. Thus, we see that for the  $\phi \rightarrow \eta\gamma \rightarrow 3\gamma$  reaction only for 0.6% of the total number of events the  $2\gamma$  quanta hit one module and in the rest 99.4% only one  $\gamma$  is registered by one module. However, for the reaction  $\phi \rightarrow \eta\gamma \rightarrow 7\gamma$  where  $\eta$  meson decays into  $3\pi^0$  the situation changes drastically and already in 6.3% cases there is two or more  $\gamma$  quanta hitting the module.

In the situation where more than one photon hit the calorimeter module it is possible that merging effect will appear for some distances between hit positions of particles on the surface. The estimations of the order of multiplicity effect was shown in Fig. 33 and Fig. 32. In the following we will describe the distribution of the distance between the  $\gamma$  quanta in the case when two  $\gamma$  hits the module. This result is relevant in view of the reconstruction possibilities of the clustering algorithm (see Fig. 33 and Fig. 32). The result for the  $\eta \rightarrow 3\pi^0$  is shown in Fig. 46. The corresponding reactions are written inside the figures. And the result for the  $\eta' \rightarrow 3\pi^0$  is shown in Fig. 47.

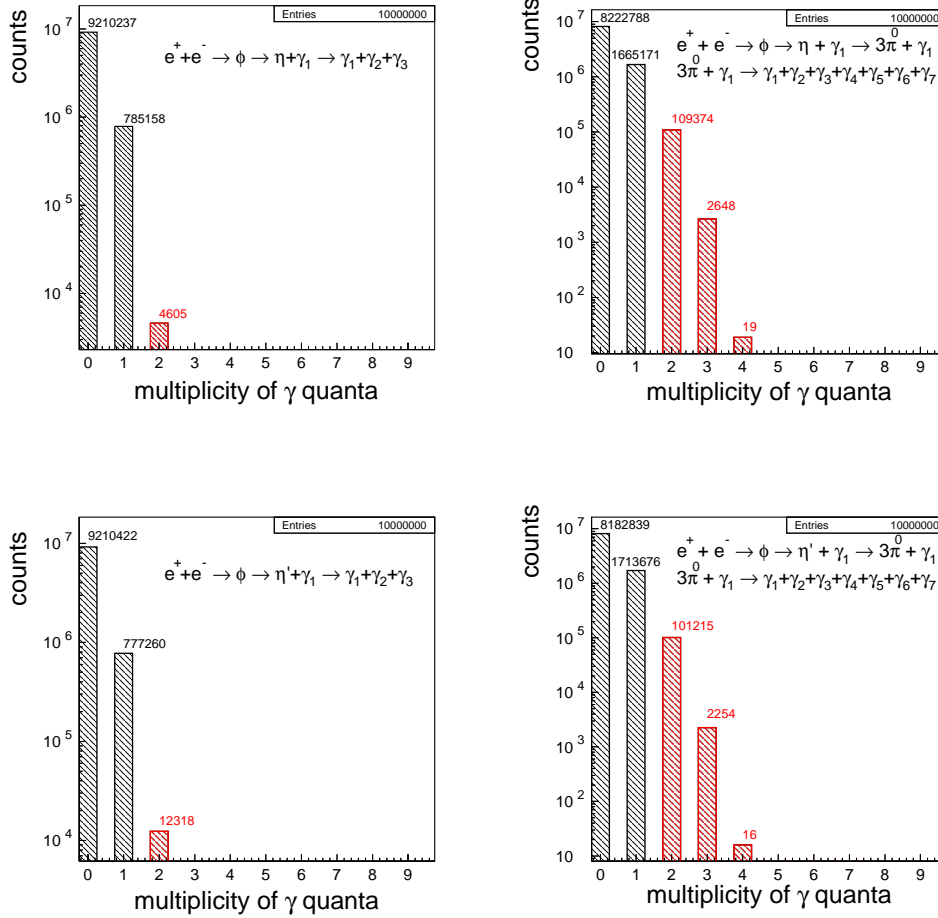


Figure 45: The multiplicity of the  $\gamma$  quanta on a single calorimeter module. For reactions described in the figure.

The distribution determined for the  $\eta'$  is not very intuitive. The maximum at 1.7 m is due to the fact that the pions from the  $\eta'$  decay are very fast and both  $\gamma$  quanta from one pion can hit one module. The pion decays immediately in the target and the distance between the two  $\gamma$  quanta from its decay at the calorimeter surface is indeed around 1.7 m.

We did also one more check by decreasing in the simulations the mass of the pion to 10 MeV. In such a case these "pions" are much faster and the laboratory angle between gamma quanta is decreasing significantly, and the distance between them in the calorimeter is as expected to be much smaller. The result of this simulation is shown in Fig. 48.

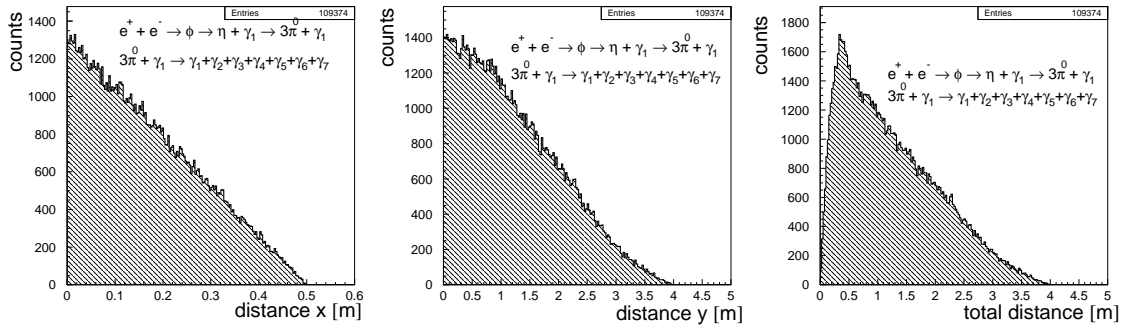


Figure 46: Distance between two gamma quanta from  $\eta \rightarrow 3\pi^0$  in one calorimeter module.

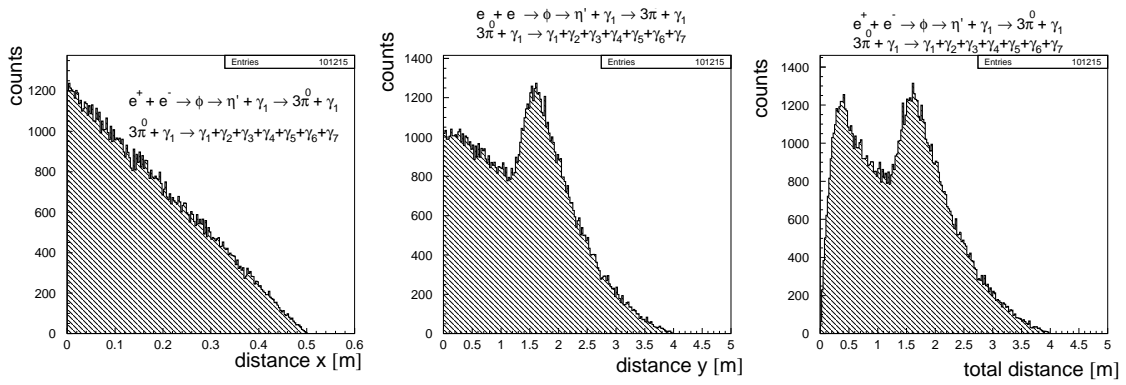


Figure 47: Distance between two  $\gamma$  quanta from reaction  $\eta' \rightarrow 3\pi^0$  on one calorimeter module.

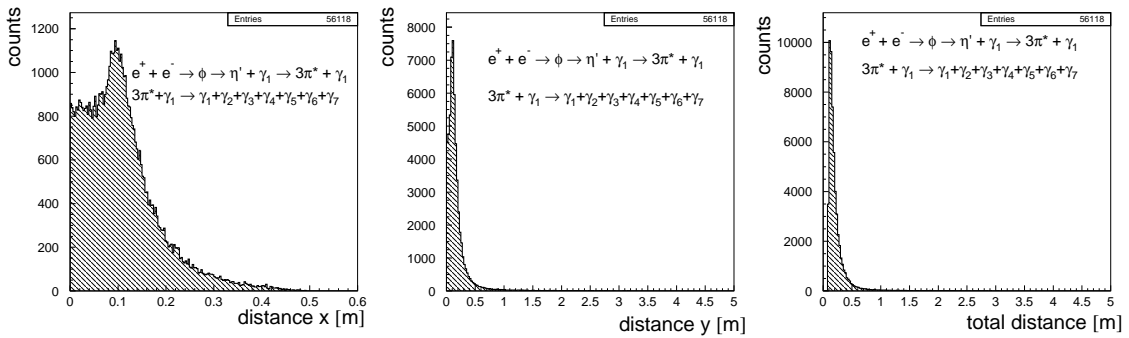


Figure 48: Distance between two  $\gamma$  quanta on one calorimeter module for reactions as depicted in the figures assuming that the "pion" mass is equal to 10 MeV.

## F Example of the event reconstruction for $e^+e^- \rightarrow \phi \rightarrow \eta\gamma \rightarrow 3\pi^0\gamma \rightarrow 7\gamma$ reaction

The capabilities of the prepared program to reproduce a merging and splitting effects in light output from scintillating fibers are illustrated in Fig. 49.

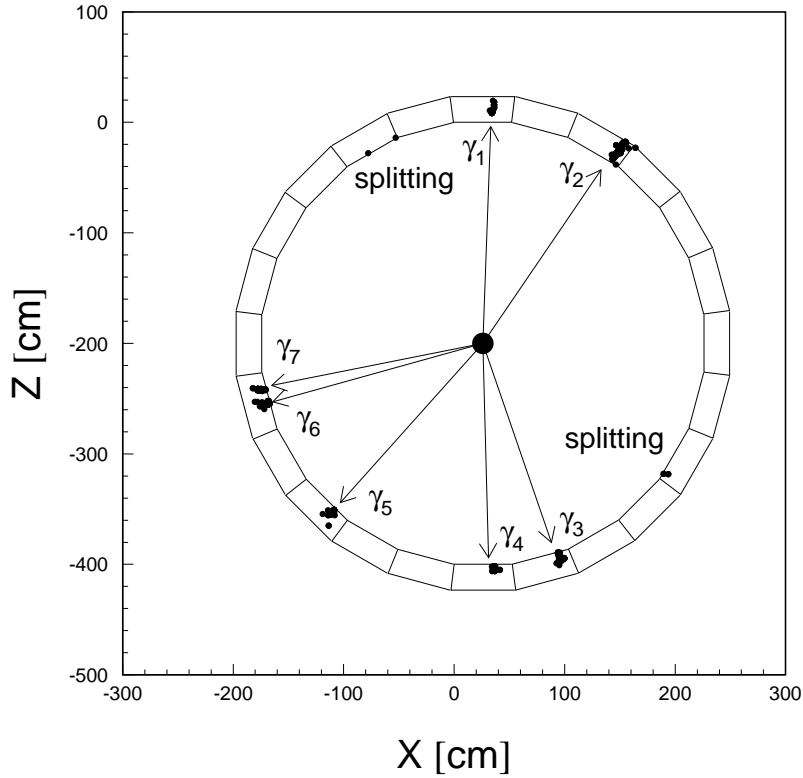


Figure 49: Splitting of energy deposits in the barrel calorimeter.

One can see seven significant energy deposits belonging to 7 photons from the  $e^+e^- \rightarrow \phi \rightarrow \eta\gamma \rightarrow 3\pi^0\gamma \rightarrow 7\gamma$  reaction, and also some small deposits of energy which don't originate directly from photons are well seen. The splitted energy deposits may cause reconstruction of the false clusters. On the other hand two very close tracks of photons (near  $z = -250$  cm) may be reconstructed as one merged cluster since the distance between particles is only about 4 cm, leading with a large probability to false reconstruction (see Fig. 49). After simulating the energy response of the scintillating fibers, on 24 modules with FLUKA, we extended appropriately the DIGICLU program in order to perform reconstruction of signals from photomultipliers on the whole barrel calorimeter.

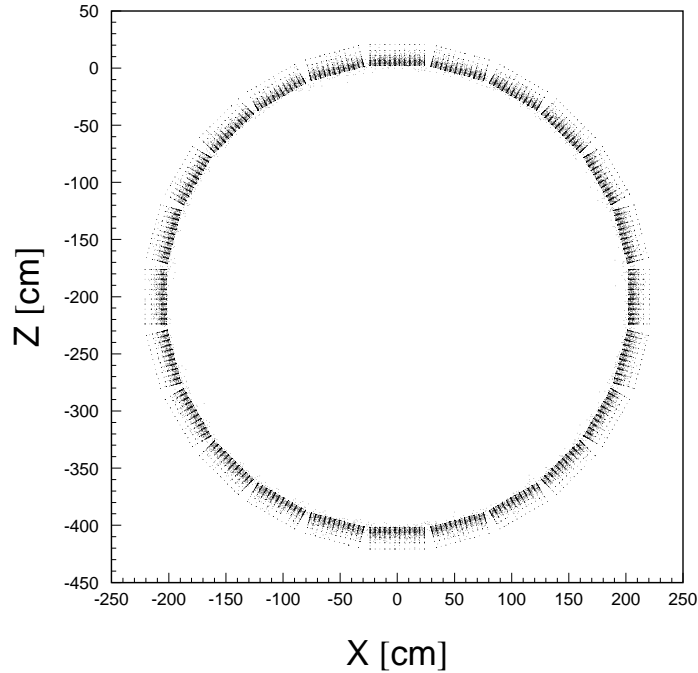


Figure 50: Reconstruction of clusters for reaction:  $e^+e^- \rightarrow \phi \rightarrow \eta\gamma \rightarrow 3\pi^0\gamma \rightarrow 7\gamma$ . Statistics is equal to 1000 events.

Fig. 50 presents distribution of reconstructed clusters on the barrel part of the calorimeter for the 1000  $e^+e^- \rightarrow \phi \rightarrow \eta\gamma \rightarrow 3\pi^0\gamma \rightarrow 7\gamma$  events simulated with vertex generator and FLUKA program. One can see that the clusters aren't reconstructed on the edges of modules.

## G Energy deposition as a function of azimuthal angle

We studied energy deposits in scintillating fibers as a function of the azimuthal angle of  $\gamma$  quanta produced in the interaction region. The results for the upper part of barrel calorimeter is shown in Fig. 51.

One can see that at the edges of the module a maximum of the energy deposits appears. To some extent it may be explained by the fact that on the edges the value of the solid angle for the same  $\phi$  angle interval is larger than in the middle (see Fig. 52).

In the simulations we did not include fibers which were near the edge since in a real detector the trapezoid shape of the module was accomplished by cutting some parts from rectangular piece [11] and hence the scintillating fibers at the sides were broken.

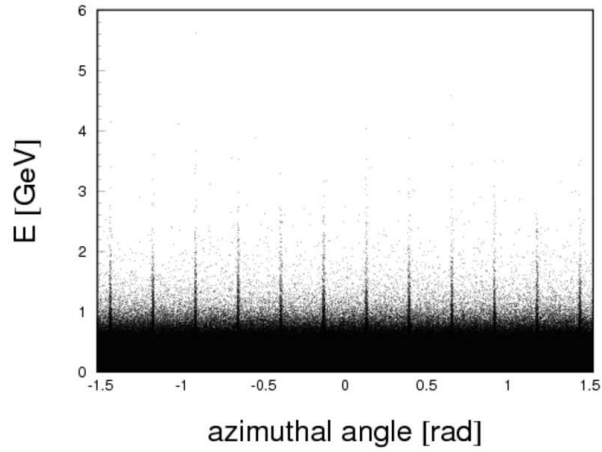


Figure 51: Energy deposits on the upper half of the barrel calorimeter as a function of cylindrical angle.

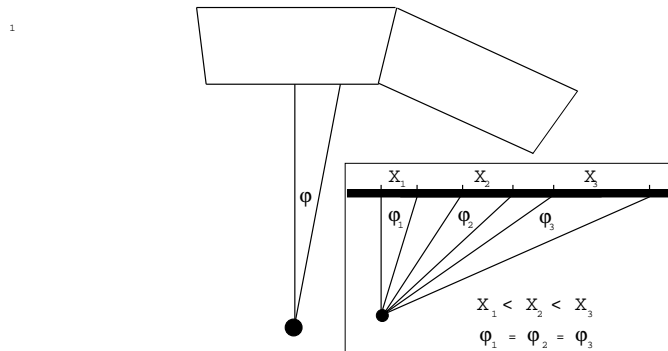


Figure 52: Schematic view of the  $\phi$  angle distribution.

In Fig. 53 one can see that for value of an angle around 0.15 rad particles didn't deposited energy. This is because this position is exactly between the edge of the first and second trapezoid modules.

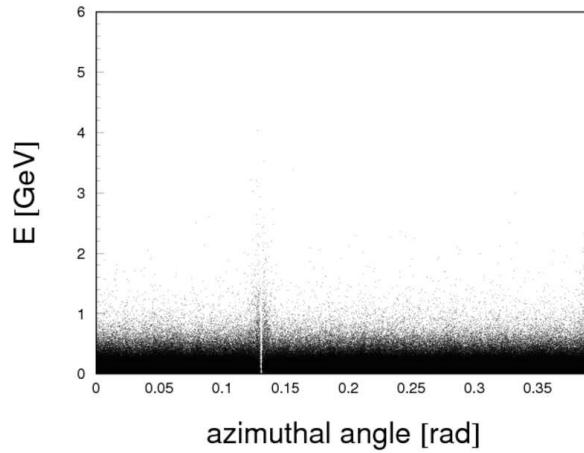


Figure 53: Energy deposits on the barrel calorimeter as function of the cylindrical angle in the range from 0 to 22.5 degree.

## H Definition of the coordinate system

The coordinate systems which were used in simulations are shown in Fig. 54. The blue axis denote the frame which was used for simulations with FLUKA and with the VERTEX GENERATOR. The red coordinate system which is the same as coordinate frame of the KLOE detector has been used in simulations of clusterization effects and simulations of the photomultipliers response with DIGICLU<sup>9</sup>. Throughout this thesis we plot all figures using the coordinate frame of the FLUKA.

---

<sup>9</sup>Digiclu frame is called the reconstruction geometry system.

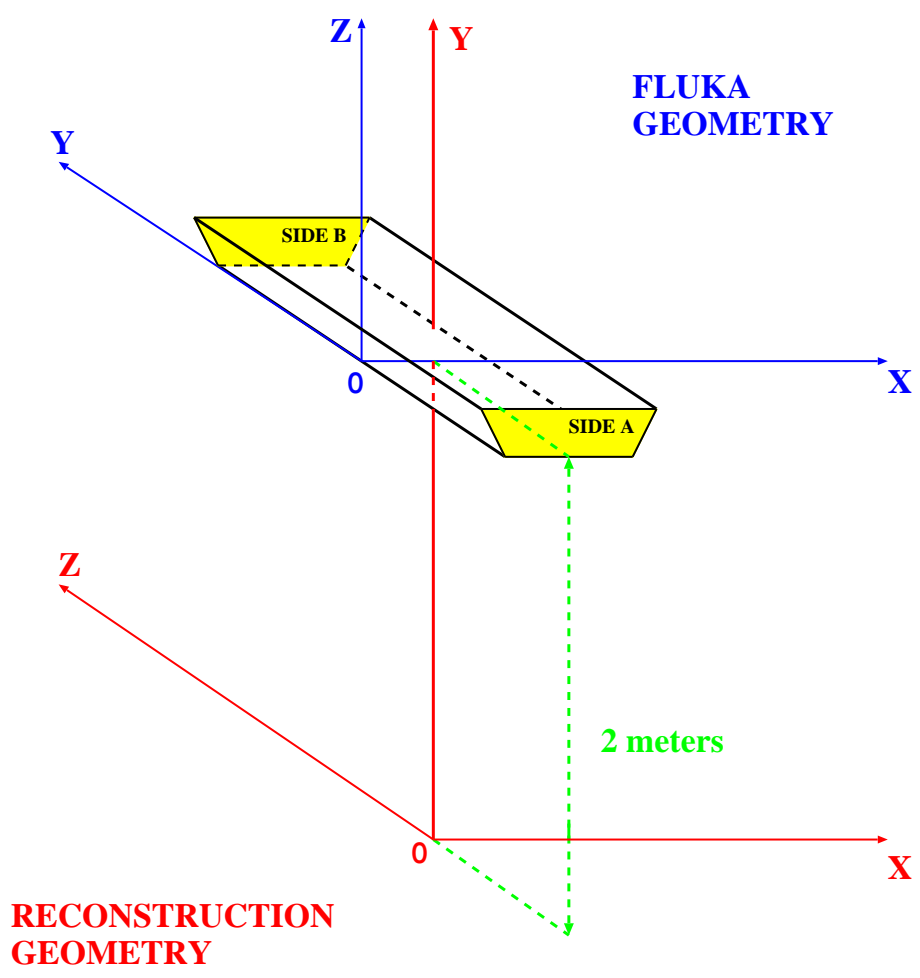


Figure 54: The coordinate systems used in simulations.

The world is given to me only once, not one existing and one perceived. Subject and object are only one. The barrier between them cannot be said to have broken down as a result of recent experience in the physical sciences, for this barrier does not exist.

Erwin Schrödinger (1887 - 1961)

Education is what remains after one has forgotten everything he learned in school.

Albert Einstein (1879 - 1955)



# Acknowledgment

At first I wish to thank Prof. dr hab. Paweł Moskal for organizing for me an additional place in travel to COSY Summer School in the year 2006. Since this event my real adventure with physics has begun. I also would like to thank you Paweł for great patience in checking this diploma thesis, for giving me a chance to study a wonderful world of particle physics, for learning me to ask myself why, and in which purpose I do my present job. And for many suggestions in the moments when I didn't know what I should do in the next step. And of course for coffees and discussions about many interesting topics.

I would like to thank dr Biagio Di Micco for many hours of working together with FLUKA geometry, with reconstruction of particles on the 24 modules of the barrel calorimeter. I am greatly indebted to you for sitting in Frascati till late evening and trying to explain me where I should look for mistakes, and of course for great patience.

I would like to thank dr Anna Ferrari for explaining me Birk effect and details related with machinery of FLUKA Monte Carlo. Also I am very grateful to you for checking this thesis and for reassuring when I was very tired.

I am very grateful to Dr Antonio Passeri for financial support of my stay in Frascati, for very nice atmosphere during the work and for help with numbering of channels in cosmic ray displayer.

I wish to thank Dr Catherina Bloise for letting me work in Laboratori Nazionali di Frascati and for financial support of my stays in Frascati. Also I am very grateful for nice atmosphere in the work.

I would like to thank Dr Federico Nguyen for patience when I was talking with Biagio all the time and disturbed him in his work, and for talkig during the lunch about football players and situation in the group during eliminations.

I wish to thank Master of Science Simona Bocchetta for nice atmosphere during the work.

I would like to thank Prof. dr hab. Bogusław Kamys for financial support of my stays in Jülich and in Frascati and for teaching me how to understand nucleus complex reactions.

I am very gratefull to Prof. dr hab. Lucjan Jarczyk for pertinent suggestions and remarks on thursdays meeting in Nuclear Physics Division of the Jagiellonian University.

I ma very grateful to Master of Science Marcin Zieliński for two years of common

work in 222 room in Nuclear Physics Division. For these two years I had got always great support from your side in all situations in my life. I would like to thank for discussions, coffees and wonderful atmosphere during the work in this room.

I wish to thank Master of Science Wojciech Krzemień for many discussions and help in my professional and private life. Also I am very grateful for working with you.

I would like to thank Dr Marek Jacewicz for discussions and coffees.

I thank Master of Science Joanna Przerwa and Master of Science Paweł Klaja for coffees, cakes and discussions about military weapons used during the Second World War.

I thank Master of Science Eryk Czerwiński for many explanations related with his work and patience in precise checking of this diploma thesis.

I would like to thank all the people from COSY-11 group and working in room 222 for wonderful atmosphere during the work. Especially, I have in my mind: Master of Science Dagmara Rozpędzik, Master of Science Barbara Rejdych, Dr Rafał Czyżykiewicz, Ewelina Czaicka, Jakub Bożek and Michał Silarski.

On my personal side I would like to thank my family: my parents Lucyna and Józef Zdebik and my brother Rafał for love, patience and support during many last years.

I thank very much Master of Science Izabela Perużyńska for being close to me in hard moments, in my life.

And at the end I would like to thank all people without whom this thesis would never be accomplished, and with whom I could work with pleasure in Kraków, Frascati and Jülich.

## References

- [1] J. Lee-Franzini and P. Franzini, e-Print: hep-ex/0702016v2, (2007).
- [2] D.H. Perkins, *Wstęp do Fizyki Wysokich Energii*, PWN, Warszawa, (1989).
- [3] R. Beck et al., KLOE-2 Letter of Intent, (2006),  
<http://www.lnf.infn.it/lnfadmin/direzione/roadmap/LoIKLOE.pdf>
- [4] P. Ciambore, A. Passeri, *The KLOE calorimeter front end electronics*, Frascati Physics Series Vol. XXI, (2000), pp. 161-167.
- [5] M. Palutan, *The KLOE calorimeter trigger*, Frascati Physics Series Vol. XXI, (2000), pp. 169-176.
- [6] B. Di Micco, Ph. D. Thesis, Roma Tre University, (2004).
- [7] M. Zobov, e-Print: arXiv:0709.3696, (2007).
- [8] V. Lucherini et al., Nucl. Instr. & Meth. in Phys. Res. **A 496** (2003) 315-324.
- [9] M. Agnello et al., Nucl. Instr. & Meth. in Phys. Res. **A 570** (2007) 205-215.
- [10] D. Alesini et al., LNF-06/33 (IR), (2006).
- [11] M. Adinolfi et al., Nucl. Instr. & Meth. in Phys. Res. **A 482** (2002) 364-386.
- [12] M. Adinolfi et al., Nucl. Instr. & Meth. **A 488** (2002) 51.
- [13] F. Ambrosino et al., e-Print: physics/0404100v1, (2004).
- [14] S. Dell’Agnello, *The KLOE detector*, Frascati Physics Series Vol. XVI, (1999), pp. 381-391.
- [15] KLOE experiment homepage, <http://www.lnf.infn.it/kloe/>
- [16] M. Adinolfi et al., Nucl. Instr. & Meth. in Phys. Res. **A 494** (2002) 326-331.
- [17] D. Domenici et al., Frascati Physics Series XLVI (2008), in print.
- [18] G. Bencivenni et al., *The Full Scal Prototype of the Cylindrical-GEM Detector as Inner Tracker in KLOE2*, Laboratori Nazionali di Frascati - INFN Via Enrico Fermi 40, I-00044 Frascati, Italy, (2008).

- [19] D. Domenici, *The upgrade of the KLOE detector: KLOE2*, Frascati Physics Series Vol. XLVI (2007), pp. 000-000.
- [20] G. Bencivenni, D. Domenici *An ultra-light cylindrical GEM detector as inner tracker at KLOE-2*, Laboratori Nazionali di Frascati - INFN, Frascati, Italy, (2007).
- [21] G. Bencivenni, D. Domenici, Nucl. Instr. & Meth. **A 581** (2007) 221.
- [22] G. Bencivenni et al., Nucl. Instr. & Meth. **A 572** (2007) 168.
- [23] G. Venanozi *The Physics case of DAFNE-2*, XXXI International Conference of Theoretical Physics "Matter To The Deepest" Ustron, Poland, (2007).
- [24] A.D'Angelo, *Progress Report on the  $\gamma\gamma$  tagger*, Laboratori Nazionali di Frascati - INFN, Frascati, Italy, (2007).
- [25] M. Adinolfi et al., Nucl. Instr. & Meth. in Phys. Res. **A 483** (2002) 649-659.
- [26] R. Beck et al., A proposal for the roll-in of the KLOE-2 detector, INFN Frascati, (2007),  
[http://www.lnf.infn.it/kloe/kloe2/roll/rollin\\_proposal.pdf](http://www.lnf.infn.it/kloe/kloe2/roll/rollin_proposal.pdf)
- [27] F. James, *Monte Carlo phase space*, CERN 68-15 (1968).
- [28] A. Fassò et al., e-Print: hep-ph/0306267v1 (2003).
- [29] A. Ferrari et al., *Fluka: a multi-particle transport code*, CERN, (2005).
- [30] J. Ranft, Phys. Rev. **D 51** (1995) 64-84.
- [31] G. Battistoni et al., e-Print: hep-ph/0612075v1, (2006).
- [32] FLUKA organization homepage,  
<http://www.fluka.org>
- [33] A. Ferrari et al., *Status of the KLOE EmC Simulation with FLUKA*, KLOE-2 meeting, LNF July 25<sup>th</sup>, (2006),  
[http://www.lnf.infn.it/kloe/kloe2/calorimeter/20060725\\_ferrari.ppt](http://www.lnf.infn.it/kloe/kloe2/calorimeter/20060725_ferrari.ppt)
- [34] B. Di Micco et al., Nuclear Physics B (Proc. Suppl.) **172** (2007) 243-245.
- [35] M. Anelli et al., Nucl. Instr. & Meth. in Phys. Res. **A 581** (2007) 368-372.

- [36] J.B. Birks, *The Theory and Practice of Scintillation Counting*, Pergamon Press, London, (1964).
- [37] GEANT, Detector Description and Simulation Tool,  
<http://wwwasdoc.web.cern.ch/wwwasdoc/pdfdir/geant.pdf>
- [38] S. Agostinelli et al., Nucl. Instr. & Meth. in Phys. Res. **A 506** (2003) 250-303.
- [39] R. Leo, *Techniques for Nuclear and Particle Physics Experiments*, Springer-Verlag, Berlin Heidelberg, New York, London, Paris, Tokyo, (1987).
- [40] M. N. Peron and P. Cassette, Nucl. Instr. & Meth. in Phys. Res. **A 369** (1996) 344-347.
- [41] G. D. Badhwar et al., Nucl. Instr. & Meth. **57** (1967) 116-120.
- [42] A. Ferrari, Dipartimento di Fisica dell'Università e Sezione INFN, "Roma Tre", Italy, private communication (2008).
- [43] E. Ambrosino et al., e-Print: hep-ex/0603056v2, (2007).
- [44] G. Battistoni homepage,  
<http://www.mi.infn.it/~battist/>
- [45] FLAIR project homepage,  
<http://www.fluka.org/flair/index.html>
- [46] J.Zdebik et al., *Implementation of the geometry of the Barrel Calorimeter with FLUKA*, KLOE-2 General Meeting, LNF 8<sup>th</sup>, (2008),  
[http://www.lnf.infn.it/kloe/kloe2/agenda\\_8May08.htm/](http://www.lnf.infn.it/kloe/kloe2/agenda_8May08.htm/)
- [47] A. Di Domenico, Dipartimento di Fisica, Università "La Sapienza" and Sezione INFN, Italy, private communication, (2008).
- [48] F. Nguyen, Dipartimento di Fisica, Università "Roma Tre" and Sezione INFN, Italy, private communication (2008).
- [49] W. Kim, *The Clustering Algorithm for the KLOE Calorimeter*, Laboratori Nazionali di Frascati, I-00044 Frascati, Italy, (1995).
- [50] B. Di Micco, Dipartimento di Fisica, Università "Roma Tre" and Sezione INFN, Italy, private communication (2008).

- [51] E. Czerwiński, Jagiellonian University, Poland, private communication (2008).
- [52] J. Filipowicz, Laboratorium Fizyki I, Uniwersytet Warszawski,  
[http://www.if.pw.edu.pl/labfiz1p/cmsimple2\\_4/1instrukcje\\_pdf/21.pdf](http://www.if.pw.edu.pl/labfiz1p/cmsimple2_4/1instrukcje_pdf/21.pdf)
- [53] A. Strzałkowski, *Wstęp do Fizyki Jądra Atomowego*, PWN, Warszawa, (1979).
- [54] E. Czerwiński and B. Di Micco, private communications (2007-2008).
- [55] S. Miscetti, Laboratori Nazionali di Frascati dell'INFN, Frascati, Italy, private communication (2008).
- [56] R. Nowak, *Statystyka dla fizyków*, Wydawnictwo Naukowe PWN, Warszawa, (2002).
- [57] R. Zieliński, *Metody Monte Carlo*, Wydawnictwo Naukowo-Techniczne, Warszawa, (1970).
- [58] J.M. Thijssen, *Computational Physics*, Cambridge University Press, (1999).
- [59] Particle Data Group, W. M. Yao et al., *J. Phys. G* **33**, (2006) 1.
- [60] A. Di Domenico, *High quantum efficiency PM upgrade: overview, status of Hamamatsu R&D, and MC studies on  $\gamma$  efficiency and  $K_{S13}$* , Symposium on KLOE-2 Calorimeter 27-30<sup>th</sup> March, Cracow, (2008),  
[http://www.lnf.infn.it/kloe/kloe2/calorimeter/symposiumcracow/didomenico\\_cracow\\_web.pdf](http://www.lnf.infn.it/kloe/kloe2/calorimeter/symposiumcracow/didomenico_cracow_web.pdf)
- [61] P. Moskal, Jagiellonian University, Poland, private communication (2008).
- [62] <http://wwwinfo.cern.ch/asd/paw/>